Commun. Comput. Phys.
doi: 10.4208/cicp.140213.210214a

Vol. **16**, No. 2, pp. 403-439
August 2014

Robust Conservative Level Set Method for 3D Mixed-Element Meshes — Application to LES of Primary Liquid-Sheet Breakup

Thibault Pringuey* and R. Stewart Cant

CFD Laboratory, Department of Engineering, University of Cambridge, UK.

Received 14 February 2013; Accepted (in revised version) 21 February 2014

Available online 21 May 2014

Abstract. In this article we detail the methodology developed to construct an efficient interface description technique — the robust conservative level set (RCLS) — to simulate multiphase flows on mixed-element unstructured meshes while conserving mass to machine accuracy. The approach is tailored specifically for industry as the three-dimensional unstructured approach allows for the treatment of very complex geometries. In addition, special care has been taken to optimise the trade-off between accuracy and computational cost while maintaining the robustness of the numerical method. This was achieved by solving the transport equations for the liquid volume fraction using a WENO scheme for polyhedral meshes and by adding a flux-limiter algorithm. The performance of the resulting method has been compared against established multiphase numerical methods and its ability to capture the physics of multiphase flows is demonstrated on a range of relevant test cases. Finally, the RCLS method has been applied to the simulation of the primary breakup of a flat liquid sheet of kerosene in co-flowing high-pressure gas. This quasi-DNS/LES computation was performed at relevant aero-engine conditions on a three-dimensional mixed-element unstructured mesh. The numerical results have been validated qualitatively against theoretical predictions and experimental data. In particular, the expected breakup regime was observed in the simulation results. Finally, the computation reproduced faithfully the breakup length predicted by a correlation based on experimental data. This constitutes a first step towards a quantitative validation.

AMS subject classifications: 65M08, 76-04, 76N99

Key words: Multiphase flow, level set method, flux limiter, MULES, WENO scheme, three-dimensional, unstructured mesh, mixed element, conservative method, atomisation, primary breakup, flat sheet breakup.

*Corresponding author. *Email address:* tp299@cam.ac.uk (T. Pringuey)

1 Introduction

Multiphase flows are encountered in a very broad variety of fields ranging from fundamental physics to geophysics and engineering. As a result, the numerical simulation of multiphase flows and in particular, the modelling of atomisation, has applications in many industries such as: aeronautics, automotive engineering, pharmaceutical, power generation, petro-chemical, manufacturing and agriculture.

In particular, aero-engines rely on air-blast atomisers to inject the kerosene in combustion chambers. The kerosene is generally injected as an annular liquid sheet sheared on either side by a faster co-flowing gas stream. This sheet undergoes a series of instabilities (longitudinal and transverse) which lead to the fragmentation of the liquid bulk into liquid structures that further disintegrate into droplets. This initial process of the atomisation is called the primary breakup and occurs in the vicinity of the injection point. As the prediction of fuel sprays in gas turbines is of critical importance to maximise the combustion efficiency and reduce the pollutant emissions from aviation, aero-engine manufacturers are investing in the development of numerical methods to model the injection process.

Various numerical methods have been developed for the simulation of multiphase flows and the most popular ones can be categorised into two groups known as moving-grid methods and fixed-grid methods. The moving-grid methods [22, 34, 49] treat the interface between the two phases as a boundary between two sub-domains of the mesh. In the case of large deformations of the interface this approach generally requires remeshing and becomes quite cumbersome when topological changes occur. The fixed-grid methods can either describe the interface explicitly or implicitly. The explicit description of the interface typically involves the solution of the flow properties on a fixed grid, together with the Lagrangian transport of a web of massless particles representing the interface. This approach using marker particles — also called the front tracking method [20, 43, 59, 61] — generally provides a precise location for the interface and also offers better control of the interfacial topology changes. However, its extension to 3D is notoriously difficult.

As implicit interface description methods are able to handle changes of interface topology automatically, they offer great potential for the simulation of atomisation. One of the most popular approaches in this category is the Volume Of Fluid (VOF) method [11,23,36] which captures the interface through the transport of the volume fraction. The volume fraction represents the volume occupied by the liquid within a computational cell. Another widely used approach is the Level Set (LS) method [40, 41, 51] which is based on the transport of a continuous function $\phi(\mathbf{x},t)$ by the underlying velocity field. In this framework, the level set (usually $\phi_\Gamma = 0$) of the function ϕ is taken to represent the interface and ϕ takes values below ϕ_Γ in one fluid and above ϕ_Γ in the other. From a numerical point of view, a smooth function is desirable and ϕ is generally taken to be equal to the signed distance from the interface. The main challenge in developing an interface description method is to produce an implicit technique that conserves mass (like Volume

of Fluid) while providing an accurate prediction of the interface location (like Level Set) and remaining robust.

More recently, hybrid methods have been produced which combine the advantages of several different approaches. In particular, these include: Marker-LS (see [16]), Marker-VOF (see [33]) and LS-VOF (see [6,35,56,62]). However, these hybrid approaches can be unwieldy, expensive and limited to the resolution of simple geometries.

Building upon recent progress in the modelling of multiphase flows, it has proved to be possible to simulate the process of atomisation in basic geometrical configurations (see [2,10,13,19,28,35]). However, the geometries modelled are still far from the complexity of the injection devices typically encountered in actual gas turbines. In order to bridge this gap, the present work has focussed on the generation of an efficient interface description technique designed to simulate the fuel injection process in real industrial systems.

Real engineering problems are characterised by the complexity of the geometry and the limited amount of human and computing resource available for the whole numerical study. As a result, an industrially-relevant modelling capability must be compatible with the use of unstructured computational grids. In addition, due to the limited amount of resource available, it is essential to base the modelling tool on numerical methods that provide the best trade-off in terms of accuracy (mass conservation and interface location) against computational cost.

In order to satisfy these requirements, the work presented in this article has focussed on the development of a novel numerical method — the Robust Conservative Level Set (RCLS) method — to transport the interface efficiently on unstructured grids, while also conserving mass. This approach is based on the Conservative Level Set (CLS) method of Olsson et al. [37,38] which generally offers a better trade-off between mass-conservation and computational cost than other interface-description methods — including state-of-the-art Coupled Level Set-VoF (see for example [35]). Our novel interface capturing technique has been implemented in parallel and in C++ using the framework provided by the open source CFD tool kit OpenFOAM [64].

This article first provides a brief overview of the RCLS method and then describes the main building blocks of the interface description technique. In particular, the transport of the level set scalar is detailed in Section 2.1, the calculation of the interface normal is presented in Section 2.3, while details of the flux limiter algorithm are given in Appendix A. Then, the performance of the RCLS method is compared with established multiphase numerical methods in Section 3.1 and the modelling capability is demonstrated on typical two-phase flow problems in Section 3.2. Finally, the RCLS method is demonstrated on the primary breakup of a flat liquid sheet of kerosene in co-flowing high-pressure gas (see Section 4). This test case is performed at relevant aero-engine conditions on a three-dimensional mixed-element unstructured mesh, following a "quasi-DNS/LES" approach [21]. The results obtained with the modelling capability are compared against experimental data [17] in Section 4.2.

2 Numerical formulation

The level set field transported, φ, can be initialised as a hyperbolic tangent profile of the signed distance function from the interface (ϕ). Introducing ϵ, a coefficient controlling the thickness of the interface, the field φ is given by:

$$\varphi = \frac{1}{2}\left(1+\tanh\left(\frac{\phi}{2\epsilon}\right)\right). \tag{2.1}$$

With such a definition for the level set field φ, the phase boundary is located at $\varphi = \frac{1}{2}$. Although the hyperbolic tangent profile localises the phase transition in the close vicinity of the interface, φ only tends to zero or unity at an infinite distance in, respectively, the gas phase or the liquid phase.

The level set field φ is identified with a smeared out liquid volume fraction and we are taking advantage of the constant thickness of the interface to apply the surface tension via the Continuum Surface Force method. As a result the material properties are given by:

$$\begin{cases} \rho = \rho_{gas} + (\rho_{liq} - \rho_{gas})\,\varphi, \\ \mu = \mu_{gas} + (\mu_{liq} - \mu_{gas})\,\varphi. \end{cases} \tag{2.2}$$

As the interface is of constant thickness, this method is analogous to a Phase Field Method (see for example [27]). Therefore, it offers the possibility to implement additional equations to describe the interface behaviour on a mesoscopic scale.

2.1 Transport of the level set

2.1.1 Mathematical formulation

In the general case, the transport of the liquid volume fraction φ can be expressed by introducing the velocity vector $\mathbf{u} = (u,v,w)$:

$$\frac{\partial \varphi}{\partial t} + \mathbf{u}\cdot\nabla\varphi = 0. \tag{2.3}$$

As we are assuming an incompressible framework, (2.3) can be re-written as the following hyperbolic conservation law:

$$\frac{\partial \varphi}{\partial t} + \nabla\cdot(\varphi\mathbf{u}) = 0. \tag{2.4}$$

Even high-order numerics such as the WENO scheme[†] described in [45,46] will eventually diffuse the interface. As a result, there is a need to re-initialise the level set profile φ to maintain the interface thickness constant. To achieve that, a compressive flux is applied normally to the interface in the transition region. Because the compressive flux

[†]We refer the interested reader to [15,24,58,60,70] and references therein.

alone would reduce the interface thickness to nearly zero, leading to a less robust method, a diffusion term is added in the re-initialisation equation. This diffusion term is also applied in the direction normal to the interface, to prevent any tangential diffusion from moving the phase boundary. Introducing the interface normal, $\hat{\mathbf{n}}$, and the artificial time, τ, along which the equation is solved, the re-initialisation equation reads:

$$\frac{\partial \varphi}{\partial \tau} + \nabla \cdot (\varphi(1-\varphi)\hat{\mathbf{n}}) = \epsilon \nabla \cdot ((\nabla \varphi \cdot \hat{\mathbf{n}})\hat{\mathbf{n}}), \tag{2.5}$$

which can be re-written as the following conservation law:

$$\frac{\partial \varphi}{\partial \tau} + \nabla \cdot \Big(\big(\varphi(1-\varphi) - \epsilon(\nabla \varphi \cdot \hat{\mathbf{n}})\big)\hat{\mathbf{n}} \Big) = 0. \tag{2.6}$$

The above equation is solved to steady state, i.e. until the initial level set profile is recovered. All the way through this iterative process, the interface normal, $\hat{\mathbf{n}}$, is kept constant.

2.1.2 Finite volume discretisation

We choose to calculate the numerical fluxes using the exact Riemann solver for both (2.4) and (2.6). As the numerical formulation of the advection equation has already been given in [46], we will focus on the re-initialisation equation in this sub-section.

Outline of the numerical formulation In order to solve Eq. (2.6), we choose to view it as a hyperbolic conservation law in which the gradient $\nabla \varphi$, in the diffusion term, is considered as a constant vector field during each artificial time step m. This gradient is then updated after each iteration of the re-initialisation step. As the normal to the interface is kept constant all the way through the re-initialisation step, the dot product in the diffusion term is constant for each $\Delta\tau$. In the rest of this section, we note this constant scalar field $\varphi_{\hat{n}}^{(m)}$ for the m^{th} artificial time step, so that we have:

$$(\nabla \varphi \cdot \hat{\mathbf{n}})^{(m)} = \varphi_{\hat{n}}^{(m)}. \tag{2.7}$$

This approach incurs a "splitting error" in artificial time. However, as we are solving the re-initialisation problem to steady state, the accuracy of the artificial time evolution is not important. Also, since we use a Runge-Kutta (RK) scheme for the temporal discretisation, we introduce a stronger coupling with the diffusion term as we update the gradient field after each RK sub-step.

In [37], Olsson and Kreiss solve the above equations on Cartesian grids using a TVD scheme with a Superbee limiter. They introduce the diffusion term in the re-initialisation equation to stabilise their CLS method. With our numerical formulation — conservative finite volume WENO scheme and exact Riemann solver — only simulations involving very large density ratios ($\rho_{liq}/\rho_{gas} \approx 1000$) require the diffusion term to be stabilised.

Derivation of the numerical flux Let us consider a discretisation of the computational domain involving conforming elements E_i of volume $|E_i|$ and boundary ∂E_i. Integrating (2.6) over the element E_i leads to:

$$\iiint_{E_i} \frac{\partial \varphi}{\partial \tau} \mathrm{d}E_i + \iiint_{E_i} \nabla \cdot \left(\left(\varphi(1-\varphi) - \epsilon \varphi_{\hat{n}}^{(m)} \right) \hat{\mathbf{n}} \right) \mathrm{d}E_i = 0. \tag{2.8}$$

Applying the divergence theorem to (2.8) and simplifying leads to:

$$\frac{\mathrm{d}}{\mathrm{d}\tau} \overline{\varphi}_i + \frac{1}{|E_i|} \iint_{\partial E_i} \left(\varphi(1-\varphi) - \epsilon \varphi_{\hat{n}}^{(m)} \right) \hat{\mathbf{n}} \cdot \mathbf{n} \, \mathrm{d}(\partial E_i) = 0, \tag{2.9}$$

where $\mathbf{n}$ is the outward unit vector normal to the surface ∂E_i.

Splitting the integral over the contour of the element ∂E_i into L_i integrals over the faces F_l of E_i, and introducing the outward unit vector normal to F_l: $\mathbf{n}_l$, we re-write (2.9) as:

$$\frac{\mathrm{d}}{\mathrm{d}\tau} \overline{\varphi}_i + \frac{1}{|E_i|} \sum_{l=1}^{L_i} \iint_{F_l} \left(\varphi(1-\varphi) - \epsilon \varphi_{\hat{n}}^{(m)} \right) \hat{\mathbf{n}} \cdot \mathbf{n}_l \, \mathrm{d}(F_l) = 0. \tag{2.10}$$

Introducing the coordinates of the normal to the interface $\hat{\mathbf{n}} = \left(\hat{n}_x, \hat{n}_y, \hat{n}_z \right)$, (2.6) can be re-written in terms of the coordinates (x,y,z):

$$\begin{aligned} 0 = \frac{\partial \varphi}{\partial \tau} &+ \frac{\partial}{\partial x} \left(\hat{n}_x \left(\varphi(1-\varphi) - \epsilon \varphi_{\hat{n}}^{(m)} \right) \right) + \frac{\partial}{\partial y} \left(\hat{n}_y \left(\varphi(1-\varphi) - \epsilon \varphi_{\hat{n}}^{(m)} \right) \right) \\ &+ \frac{\partial}{\partial z} \left(\hat{n}_z \left(\varphi(1-\varphi) - \epsilon \varphi_{\hat{n}}^{(m)} \right) \right) \end{aligned} \tag{2.11}$$

such that the fluxes $F(\varphi)$, $G(\varphi)$ and $H(\varphi)$ in respectively the x, y and z directions read:

$$\begin{cases} F(\varphi) = \hat{n}_x \left(\varphi(1-\varphi) - \epsilon \varphi_{\hat{n}}^{(m)} \right), \\ G(\varphi) = \hat{n}_y \left(\varphi(1-\varphi) - \epsilon \varphi_{\hat{n}}^{(m)} \right), \\ H(\varphi) = \hat{n}_z \left(\varphi(1-\varphi) - \epsilon \varphi_{\hat{n}}^{(m)} \right), \end{cases} \tag{2.12}$$

so that we have:

$$\begin{cases} \mathbf{A} = (F,G,H) \\ \quad = \left(\hat{n}_x \left(\varphi(1-\varphi) - \epsilon \varphi_{\hat{n}}^{(m)} \right), \hat{n}_y \left(\varphi(1-\varphi) - \epsilon \varphi_{\hat{n}}^{(m)} \right), \hat{n}_z \left(\varphi(1-\varphi) - \epsilon \varphi_{\hat{n}}^{(m)} \right) \right), \\ A_{n_l}(\varphi^-, \varphi^+) = \mathbf{A} \cdot \mathbf{n}_l. \end{cases} \tag{2.13}$$

The re-initialisation equation can then be expressed in the following finite volume form:

$$\frac{\mathrm{d}}{\mathrm{d}\tau} \overline{\varphi}_i + \frac{1}{|E_i|} \sum_{l=1}^{L_i} \iint_{F_l} A_{n_l} \left(\varphi^-, \varphi^+ \right) \mathrm{d}(F_l) = 0. \tag{2.14}$$

As for the linear equation and the Burgers equation (see [46]), simple manipulations of (2.11) demonstrate its rotational invariance according to:

$$\mathbf{A}\cdot\mathbf{n}_l=(F,G,H)\cdot\mathbf{n}_l=n_{lx}F+n_{ly}G+n_{lz}H=\widehat{F}, \tag{2.15}$$

where $\widehat{F}$ is the flux vector expressed in the direction n_l, the first axis of the rotated Cartesian frame (n_l,s_l,t_l). Introducing $\overline{\varphi_{\hat{n}}^{(m)}}$ the face-averaged gradient of the level set in the direction of the normal to the interface, the expression for $\widehat{F}$ reads:

$$\widehat{F}=(\hat{\mathbf{n}}\cdot\mathbf{n}_l)\left(\varphi(1-\varphi)-\epsilon\overline{\varphi_{\hat{n}}^{(m)}}\right)=\hat{n}_{n_l}\left(\varphi(1-\varphi)-\epsilon\overline{\varphi_{\hat{n}}^{(m)}}\right). \tag{2.16}$$

Therefore, the flux across F_l is given by the one-dimensional equation:

$$\frac{\partial\varphi}{\partial\tau}+\frac{\partial\widehat{F}}{\partial n_l}=0. \tag{2.17}$$

Eq. (2.17) leads to the Riemann problem:

$$\left.\begin{array}{ll}\text{PDE:} & \dfrac{\partial\varphi}{\partial\tau}+\dfrac{\partial}{\partial n_l}\left(\hat{n}_{n_l}\left(\varphi(1-\varphi)-\epsilon\overline{\varphi_{\hat{n}}^{(m)}}\right)\right)=0,\\ \text{IC:} & \varphi(n_l,0)=\varphi_0(n_l)=\left\{\begin{array}{ll}\varphi^- & \text{if } n_l<0,\\ \varphi^+ & \text{if } n_l>0.\end{array}\right.\end{array}\right\} \tag{2.18}$$

For the PDE (2.18), the characteristic speed $\lambda(\varphi)$ is given by:

$$\lambda(\varphi)=\frac{\mathrm{d}\widehat{F}}{\mathrm{d}\varphi}=\hat{n}_{n_l}(1-2\varphi) \tag{2.19}$$

Eq. (2.18) admits an exact solution:

$$\left.\begin{array}{l}\text{If } \lambda(\varphi^-)>\lambda(\varphi^+): \qquad \varphi(n_l,\tau)=\left\{\begin{array}{ll}\varphi^- & \text{if } n_l-S\tau<0,\\ \varphi^+ & \text{if } n_l-S\tau>0,\end{array}\right.\\ \text{with: } S=\frac{\Delta\widehat{F}}{\Delta\varphi}=\hat{n}_{n_l}(1-(\varphi^-+\varphi^+)).\\ \text{If } \lambda(\varphi^-)\leq\lambda(\varphi^+): \qquad \left\{\begin{array}{ll}\varphi(n_l,\tau)=\varphi^- & \text{if } \frac{n_l}{\tau}\leq\lambda(\varphi^-),\\ \lambda(\varphi)=\frac{n_l}{\tau} & \text{if } \lambda(\varphi^-)<\frac{n_l}{\tau}<\lambda(\varphi^+),\\ \varphi(n_l,\tau)=\varphi^+ & \text{if } \frac{n_l}{\tau}\geq\lambda(\varphi^+),\end{array}\right.\end{array}\right\} \tag{2.20}$$

so that the flux A_{n_l} (see (2.13)) across F_l (i.e. at $n_l=0$ with $t>0$), reads:

$$\left.\begin{aligned}
&\text{If } \lambda(\varphi^-)>\lambda(\varphi^+): \quad A_{n_l}(\varphi^-,\varphi^+)=\begin{cases}\hat{n}_{n_l}\left(\varphi^-(1-\varphi^-)-\epsilon\overline{\varphi^{(m)}_{\hat{n}}}\right) & \text{if } S>0,\\ \hat{n}_{n_l}\left(\varphi^+(1-\varphi^+)-\epsilon\overline{\varphi^{(m)}_{\hat{n}}}\right) & \text{if } S<0,\end{cases}\\
&\text{with: } S=\hat{n}_{n_l}(1-(\varphi^-+\varphi^+)).\\
&\text{If } \lambda(\varphi^-)\leq\lambda(\varphi^+):\\
&A_{n_l}(\varphi^-,\varphi^+)=\begin{cases}\hat{n}_{n_l}\left(\varphi^-(1-\varphi^-)-\epsilon\overline{\varphi^{(m)}_{\hat{n}}}\right) & \text{if } 0\leq\hat{n}_{n_l}(1-2\varphi^-),\\ \hat{n}_{n_l}\left(\frac{1}{4}-\epsilon\overline{\varphi^{(m)}_{\hat{n}}}\right) & \text{if } \hat{n}_{n_l}(1-2\varphi^-)<0<\hat{n}_{n_l}(1-2\varphi^+),\\ \hat{n}_{n_l}\left(\varphi^+(1-\varphi^+)-\epsilon\overline{\varphi^{(m)}_{\hat{n}}}\right) & \text{if } 0\geq\hat{n}_{n_l}(1-2\varphi^+).\end{cases}
\end{aligned}\right\} \tag{2.21}$$

As explained in [46], when considering non-linear hyperbolic equations such as (2.7), the Riemann problem has to be solved locally, i.e. for each point of the Gaussian quadrature. The overall flux through the face is then integrated over F_l.

2.1.3 Temporal discretisation

Noting the time variation of φ: $L(\varphi)$, the finite volume form of an hyperbolic conservation law then reads:

$$\begin{aligned}\frac{\mathrm{d}}{\mathrm{d}t}\overline{\varphi}_i&=-\frac{1}{|E_i|}\sum_{l=1}^{L_i}\iint_{F_l}A_{n_l}(\varphi^-,\varphi^+)\,\mathrm{d}(F_l)\\&=L(\varphi).\end{aligned} \tag{2.22}$$

Runge-Kutta schemes We have chosen to use Runge-Kutta schemes for both the advection and the re-initialisation steps. Introducing $\alpha_{i,k}$ and $\beta_{i,k}$, the coefficients of a general Runge-Kutta scheme, the liquid fraction at the i^{th} Runge-Kutta iteration is given by the formula below:

$$\varphi^{(i)}=\sum_{k=0}^{i-1}\alpha_{i,k}\varphi^{(k)}+\beta_{i,k}\Delta tL\left(\varphi^{(k)}\right). \tag{2.23}$$

We choose the three-stage, third-order strong-stability preserving (SSP) Runge-Kutta scheme of Shu and Osher [53]: SSP(3,3). This scheme is widely used in conjunction with WENO schemes because of its stability and accuracy [40, 63]. The coefficients of this scheme are given in Table 1. Other SSP Runge-Kutta schemes were tested (taken from [63]), but the SSP(3,3) scheme offered the best trade-off between stability, accuracy and computational cost for our numerical formulation.

The solution of the incompressible Navier-Stokes equations in OpenFOAM admits the volumetric flow rate as a variable instead of the velocity. As a result, in order to

Table 1: Coefficients of the Runge-Kutta scheme SSP(3,3) of Shu and Osher [53].

$\alpha_{i,k}$			$\beta_{i,k}$		
1			1		
$\frac{3}{4}$	$\frac{1}{4}$		0	$\frac{1}{4}$	
$\frac{1}{3}$	0	$\frac{2}{3}$	0	0	$\frac{2}{3}$

update the volumetric flow rate after the transport of the liquid volume fraction φ, it is necessary to derive the contribution to the flux for each Runge-Kutta step.

The expression for the liquid volume fraction at the end of the Runge-Kutta scheme (iteration n) can be re-written as:

$$\varphi^{(n)} = K_\alpha \varphi^{(0)} + \sum_{k=0}^{n-1} K_{\beta k} \Delta t L\left(\varphi^{(k)}\right), \tag{2.24}$$

where the coefficients K_α and $K_{\beta k}$ are functions of the coefficients of the RK scheme, $\alpha_{i,k}$ and $\beta_{i,k}$, designed such that:

$$K_\alpha = 1, \tag{2.25}$$

$$\sum_{k=0}^{n-1} K_{\beta k} = 1. \tag{2.26}$$

The contribution to the total flux of the k^{th} RK iteration has to be weighted by the coefficient $K_{\beta k}$. We have demonstrated that $K_{\beta k}$ is given by the following formula:

$$K_{\beta k} = \sum_{j=0}^{n-k-1} C_{k+j}, \tag{2.27}$$

with:

$$\left.\begin{array}{ll} j=0: & C_k = \beta_{i,k}, \\ j=1: & C_{k+1} = \alpha_{i,k+1} \times \beta_{k+1,k}, \\ j \geq 2: & C_{k+j} = \alpha_{i,k+j} \times \left(\beta_{k+j,k} + \sum\limits_{m=1}^{j-1} \alpha_{k+j,k+m} \times \dfrac{C_{m+k}}{\alpha_{i,k+m}}\right). \end{array}\right\} \tag{2.28}$$

Stability restrictions on the artificial time step As the temporal discretisation of the re-initialisation equation is performed with an explicit scheme, it is necessary to consider the stability restrictions associated with the numerical solution of (2.6). Olsson and Kreiss identify the viscous term in (2.6) as the driver of numerical instabilities and suggest the following condition [37]:

$$\Delta\tau \leq K \frac{(\Delta x)^2}{\epsilon}. \tag{2.29}$$

From numerical experiments conducted with a Runge-Kutta scheme, Olsson and Kreiss established that the stability is typically obtained with: $K = \frac{1}{4}$.

2.1.4 Addition of a flux limiter

As noted in [12, 63], WENO schemes are not necessarily Total Variation Bounded (TVB), even when coupled with a Total Variation Diminishing (TVD) Runge-Kutta time integration. However, as our conservative level set field represents the liquid volume fraction in the domain, non-physical values of φ such that $\varphi<0$ or $\varphi>1$ cannot be tolerated. Indeed, such non-physical values may worsen over millions of time steps and eventually the density, calculated from φ, may end up negative in some cells.

As a result, we decided to use the Multidimensional Universal Limiter with Explicit Solution (MULES) of Weller [39], used by default in OpenFOAM to maintain the boundedness of the VOF field. To our knowledge, this algorithm has not appeared in any publication. Appendix A presents the details of the MULES method.

2.1.5 Choice of the parameter ϵ

The main parameter of the Conservative Level Set method is the coefficient ϵ that drives the spread of the hyperbolic tangent profile in (2.1). Therefore ϵ effectively controls the thickness of the phase transition.

It is preferable to model the interface to be as thin as possible, since a sharp interface represents better the reality of the physics and involve less smearing of the material properties and the surface tension. A small ϵ is also desirable to minimize the effect of the re-initialisation step.

Nevertheless, the interface needs to have a minimal thickness, so that the gradient of φ and the interface normal are accurately calculated. A minimum value for ϵ also results from a "stability study" of the 1D re-initialisation equation. Olsson et al. performed this study for a finite element method in [38]. Following the same methodology, our stability study for the finite volume framework lead us to the same conclusion (see [44]): in order to maintain a stable solution of the re-initialisation equation, it is necessary to choose:

$$\epsilon \geq \frac{1}{2}\cdot\Delta x. \tag{2.30}$$

Just like Olsson and Kreiss, we choose to take ϵ proportional to the grid size:

$$\epsilon = C\Delta x. \tag{2.31}$$

The consequence of that choice is twofold:

- The equations solved for the transport of the liquid volume fraction change as the grid is refined.
- As Δx decreases, the profile of the conservative level set in the phase transition region is resolved using the same number of cells.

2.1.6 Initialisation of the conservative level set field

On simple test cases, the signed distance function from the interface, ϕ, may be calculated analytically so that the initial conservative level set field $\varphi^{(0)}$ can be easily derived by applying the formula (2.1) in each cell of the mesh.

If the field cannot be calculated analytically, one way to obtain $\varphi^{(0)}$ is to compute ϕ first by solving the re-distancing equation to steady state [8, 55, 57] or by using Sethian's Fast Marching Method [52]. However, none of these methods exists for general polyhedral meshes.

Another option, described by Olsson and Kreiss in [37], is to initialise φ as a VOF field — setting 0 in the cells containing gas and 1 in the cells containing liquid — and then to solve the re-initialisation equation (2.5) to steady state. This procedure will produce an initial conservative level set field of reasonable quality. For a generic distribution of liquid on a general polyhedral mesh, this is the only viable method.

2.2 Solution of the incompressible Navier-Stokes equations

As our novel interface capturing technique is implemented in OpenFOAM, the solution of the Navier-Stokes equations is performed using the same methodology as OpenFOAM's multiphase flow solver: *interFoam*. This procedure is described below.

2.2.1 Conservative formulation

The governing equations for multiphase flows with interface modelling can be found in [50]. Implementing in these equations the CSF description of the surface tension (see [7]), leads to the following conservation formulation of the incompressible Navier-Stokes equations:

$$\nabla\cdot\mathbf{u}=0, \tag{2.32}$$

$$\frac{\partial(\rho\mathbf{u})}{\partial t}+\nabla\cdot(\rho\mathbf{u}\otimes\mathbf{u})=-\nabla p+\rho\mathbf{g}+\sigma\kappa\nabla\varphi+\nabla\cdot(2\mu\mathcal{D}), \tag{2.33}$$

where the rate-of-strain tensor $\mathcal{D}$ reads:

$$\mathcal{D}=\frac{1}{2}\left(\nabla\mathbf{u}+(\nabla\mathbf{u})^T\right). \tag{2.34}$$

A modified pressure p_d is introduced to simplify the specification of the pressure boundary conditions [48]. p_d is defined by:

$$p_d=p-\rho\mathbf{g}\cdot\mathbf{x} \tag{2.35}$$

such that the formulation of the momentum equation as used in the code reads:

$$\frac{\partial(\rho\mathbf{u})}{\partial t}+\nabla\cdot(\rho\mathbf{u}\otimes\mathbf{u})=-\nabla p_d+\nabla\cdot(\mu\nabla\mathbf{u})+(\nabla\mathbf{u})\cdot\nabla\mu-(\mathbf{g}\cdot\mathbf{x})\nabla\rho+\sigma\kappa\nabla\varphi. \tag{2.36}$$

2.2.2 Pressure-velocity coupling

The incompressible Navier-Stokes equations are discretised in a semi-implicit manner such that the restriction on the time step remains low. The pressure velocity coupling is handled with the Pressure-Implicit with Splitting Operators (PISO) method of Issa [26]. This non-iterative method proceeds through a series of predictor and corrector steps that approximate the exact velocity and pressure fields with improving accuracy as the number of PISO loops increases.

2.3 Calculation of the interface normal

2.3.1 Mathematical formulation

The face-averaged gradient, $\overline{\nabla\varphi_{\mathbf{x}}}$, is required for the calculation of the interface normal, the non-linear flux and the surface tension forces. Let us recall the definition of $\overline{\nabla\varphi_{\mathbf{x}}}$ below:

$$\overline{\nabla\varphi_{\mathbf{x}}}=\frac{1}{|F_l|}\iint_{F_l}\nabla\varphi_{\mathbf{x}}\,\mathrm{d}(F_l). \tag{2.37}$$

Desjardins observed in [12] that the quality of the gradient field calculation was important to avoid spurious oscillations. To resolve this issue, we have chosen to take advantage of the polynomial reconstruction of the scalar field φ performed by the WENO scheme [46]. As the polynomial reconstruction is performed in a reference space $\boldsymbol{\xi}=(\xi,\eta,\zeta)$ — where scaling effects do not apply — the smeared out liquid volume fraction φ is approximated by a WENO polynomial according to the following formula [46]:

$$\varphi_{WENO}(\xi,\eta,\zeta)=\overline{\varphi}_0+\sum_{k=1}^{K}\tilde{a}_k\phi_k(\xi,\eta,\zeta), \tag{2.38}$$

where the $\tilde{a}_k$ are the degrees of freedom of the WENO polynomial reconstruction and the $\phi_k(\xi,\eta,\zeta)$ the basis functions of the polynomial reconstruction.

This polynomial — already calculated by the high-order WENO scheme for the linear flux of the advection equation — embeds both the essentially non-oscillatory characteristic (required to avoid the spurious oscillations mentioned by Desjardins) and high-order approximation of the gradient.

As the gradient is needed in the physical space, the Jacobian of the mapping transformation, $\mathcal{J}$, has to be introduced in the calculation, according to:

$$\nabla\varphi_{\mathbf{x}}=\left(\mathcal{J}^{-1}\right)^{T}\nabla\varphi_{\boldsymbol{\xi}}. \tag{2.39}$$

Based on equations (2.37), (2.38) and (2.39) and recalling that F_l' is the face F_l in the

mapped space, the following expression can be derived for the face-averaged gradient:

$$\overline{\nabla\varphi_{\mathbf{x}}}=\sum_{k=1}^{K}\tilde{a}_k\underbrace{\left(\frac{1}{|F_l'|}\left(\mathcal{J}^{-1}\right)^T\mathbf{v}_k\right)}_{\text{pre-computed}}, \tag{2.40}$$

where the vector $\mathbf{v}_k$ reads:

$$\mathbf{v}_k=\begin{pmatrix} A_k\iint_{F_l'}\xi^{(A_k-1)}\eta^{B_k}\zeta^{C_k}\,\mathrm{d}\left(F_l'\right)\\ B_k\iint_{F_l'}\xi^{A_k}\eta^{(B_k-1)}\zeta^{C_k}\,\mathrm{d}\left(F_l'\right)\\ C_k\iint_{F_l'}\xi^{A_k}\eta^{B_k}\zeta^{(C_k-1)}\,\mathrm{d}\left(F_l'\right)\end{pmatrix}. \tag{2.41}$$

The added cost for the above calculation is fairly small as the degrees of freedom are computed for the flux determination and since the terms multiplying the $\tilde{a}_k$ in (2.40) are precomputed.

Also, the integrals of the monomials in (2.41) are simple combinations of the volume integrals of the monomial and the surface integrals of the basis functions. Let us recall the definition of the basis functions:

$$\phi_k=\psi_k-\frac{1}{|E_i'|}\iiint_{E_i'}\psi_k\,\mathrm{d}\left(E_i'\right), \tag{2.42}$$

with: $\{\psi_k\}=\xi,\eta,\zeta,\xi^2,\xi\cdot\eta,\cdots,\zeta^r$, $k=1,\cdots,K$.

Hence the integrals of the monomials, ψ_k, involved in $\mathbf{v}_k$ can be calculated from:

$$\iint_{F_l'}\psi_k\,\mathrm{d}\left(F_l'\right)=\underbrace{\iint_{F_l'}\phi_k\,\mathrm{d}\left(F_l'\right)}_{\text{pre-computed for the flux}}-\frac{|F_l'|}{|E_i'|}\underbrace{\iiint_{E_i'}\psi_k\,\mathrm{d}\left(E_i'\right)}_{\text{pre-computed for }A_{jk}}. \tag{2.43}$$

Both of the integrations on the r.h.s. of (2.43) have already been performed: the first one for the flux calculation and the second one for the polynomial reconstruction.

2.4 Interpretation of the method

The RCLS method transports a scalar φ defined as the hyperbolic tangent profile of the signed distance to the interface. The scalar φ is transported in a conservative manner (see [46] and [44]) such that it remains conserved to machine accuracy (Lax and Wendroff

provided some theoretical background for this assertion in [32] and our numerical experiments, presented in Section 3.2 confirm it). In addition, the transition between phases, characterised by this hyperbolic tangent profile, is kept to a constant thickness.

If applied in the same spirit as Olsson and Kreiss [37] and Desjardins et al. [13], the RCLS method transports a function of the distance to the interface. The phase boundary being defined by the contour $\varphi = 0.5$, all the volume encompassed by that surface can be considered as filled with liquid. Such an interpretation of φ leads to a level set formulation of the RCLS.

However, as the interface thickness is kept constant, the scalar transported φ can be identified with the liquid volume fraction. When interpreting φ as such, the RCLS resembles a VOF method with an interface of constant thickness. The interface reconstruction generally required by VOF methods is no longer required here, as the hyperbolic tangent profile provides a smooth field to calculate the interface gradient.

The RCLS method can therefore be perceived as both a Level Set method and a Volume of Fluid method.

3 Canonical test cases

3.1 Performance of the method

This section compares the performance of the RCLS with established multiphase numerical methods:

- the VOF method of OpenFOAM: *interFoam*;
- the Accurate Conservative Level Set (ACLS) method of Desjardins et al. [12, 13].

For this comparative study, the RCLS transports the scalar field φ using a WENO3 scheme, the CLS coefficient is set to $\epsilon = 0.5\Delta x$ and the re-initialisation of the hyperbolic tangent profile is only performed every five time steps.

3.1.1 Comparison with *interFoam*

The relative performance of the transport algorithms is assessed on the following test cases (defined in [46]): Zalesak's slotted disk (on a 128^2 Cartesian mesh) and the disk in a deformation field (on a 256^2 Cartesian mesh).

As can be seen in Fig. 1, the RCLS method clearly outperforms *interFoam* on both test cases. In particular, the ligament predicted by our transport algorithm is longer and the interface is free from non-physical wiggles.

3.1.2 Comparison with ACLS

In order to compare the method of Desjardins et al. with the RCLS, we have performed the computation of the disk in a deformation field as set in [13]. It is interesting to note

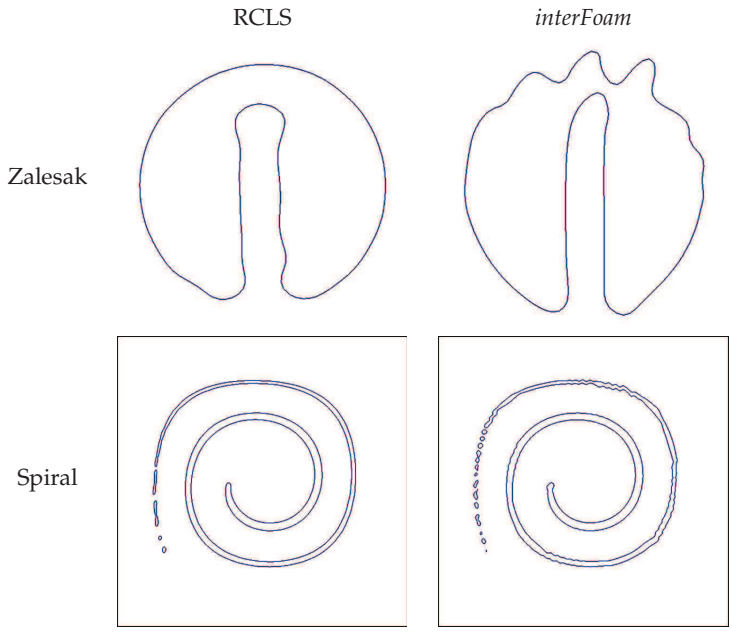

Figure 1: Performance of the transport algorithms of *interFoam* and the RCLS method — Results for Zalesak's slotted disk (Zalesak) and the disk in a deformation field (Spiral).

that this deformation field differs from that given in [46]. As in [13], we set the stream function to:

$$\psi = \frac{1}{\pi}\sin^2(\pi x)\cos^2(\pi y)\cos\left(\frac{\pi t}{T}\right), \tag{3.1}$$

with $T = 8\ s$.

The resulting velocity vector $\mathbf{u}$ reads:

$$\mathbf{u} = \left(\frac{\partial \psi}{\partial y}, -\frac{\partial \psi}{\partial x}\right). \tag{3.2}$$

As in [13], the calculation was performed on a 256^2 Cartesian mesh with a constant time step of $\Delta t = 0.002\ s$. The predicted level set contours are given in Fig. 2 at $t = \frac{T}{2}$, when the stretching is maximal. As can be seen in Fig. 2, the RCLS clearly outperforms the ACLS method on this test case.

3.2 Simulation of multiphase flows

The calculations presented in this sub-section are typical tests that assess the performance of the multiphase modelling capability. In particular, we present here the results obtained by our method on two test cases: the Rayleigh-Taylor instability and the falling drop in a pool. Through these simulations we illustrate three features of our method:

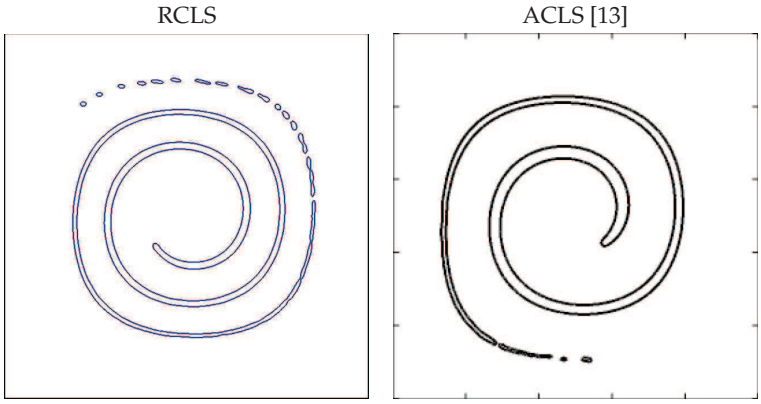

Figure 2: Performance of the transport algorithms of the ACLS and the RCLS methods — Results for the disk in a deformation field (as set in [13]).

- accuracy;
- robustness;
- ability to run on different types of mesh.

3.2.1 Rayleigh-Taylor instability

The settings for the simulation of the Rayleigh-Taylor instability are given in [47]. For this test case, the transport of the volume fraction φ was performed with our novel modelling capability (*RCLSFoam*) using the linear high-order scheme and setting the interface thickness parameter to $\epsilon = 0.5\overline{\Delta x}$. This highlights the robustness of our method which copes with a density ratio of 7.4 without resorting to a WENO treatment of the discontinuity.

Ability to capture the physics The relative performance of *RCLSFoam* with respect to OpenFOAM's multiphase flow solver (*interFoam*) is presented in Fig. 3. This figure shows the solution obtained by the two codes on the same triangular mesh made of 9234 cells, for six different times in $[0;1.5]$ seconds.

The comparison of the interface predicted by the two solvers for the first three times ($t = 0.7\ s, 0.8\ s, 0.9\ s$) demonstrates the superior performance of *RCLSFoam* on asymmetrical meshes. Indeed, while the solution predicted by our approach remains close to the reference solution obtained with an accurate front tracking method [43], *interFoam*'s predictions are unrealistically asymmetrical. This is probably due to the lower order of the numerical schemes used by *interFoam* (smaller stencils) to transport the volume fractions. It suggests that *interFoam* is not appropriate on general unstructured grids.

The solution predicted by *interFoam* for the last three times ($t = 1.25\ s, 1.4\ s, 1.45\ s$) illustrates a flaw of this solver: *interFoam* produces non-physical wiggles in the stem of the mushroom-shaped structure formed by the penetration of the denser phase into the

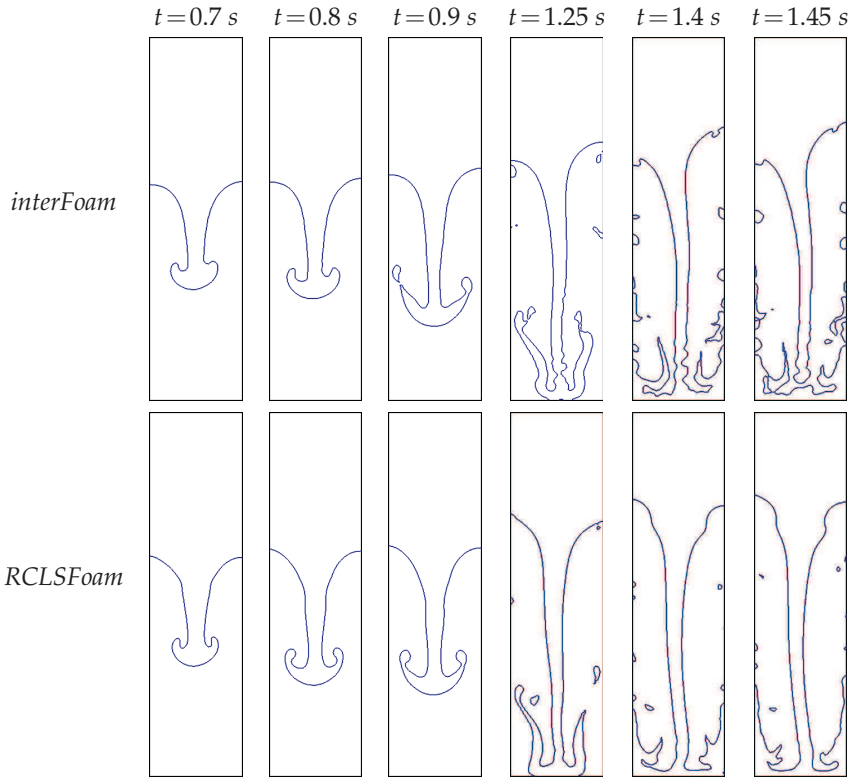

Figure 3: Interface predicted by *RCLSFoam* for the Rayleigh-Taylor instability — Comparison *RCLSFoam* vs. *interFoam*.

lighter phase. Fig. 3 shows the build up of these non-physical interfacial oscillations until they break the mushroom-shaped structure (see results for $t=1.45\ s$).

Handling of hybrid meshes *RCLSFoam*'s ability to perform accurately on different types of grid is demonstrated by comparing the solutions obtained on a triangular and a hybrid (triangles-rectangles) mesh of similar size. Fig. 4 shows the two meshes considered for this study: a triangular mesh of 9234 cells and a hybrid grid of 8580 elements. The rectangles of the hybrid mesh are distributed all along the width, in the middle portion of the domain — where the interface is initialised — and the rest of the domain is made of triangular elements.

Fig. 4 presents the volume fractions and interface predicted by *RCLSFoam* on the two meshes for five different times in $[0;1]$ second. As expected the results obtained are very similar and, thanks to the high-order scheme implemented, the method copes very well with the change of mesh type in the hybrid grid.

Small differences in the solution at time $t=1s$ can be perceived between the two computations: the interface obtained on the hybrid mesh is slightly more symmetrical. This

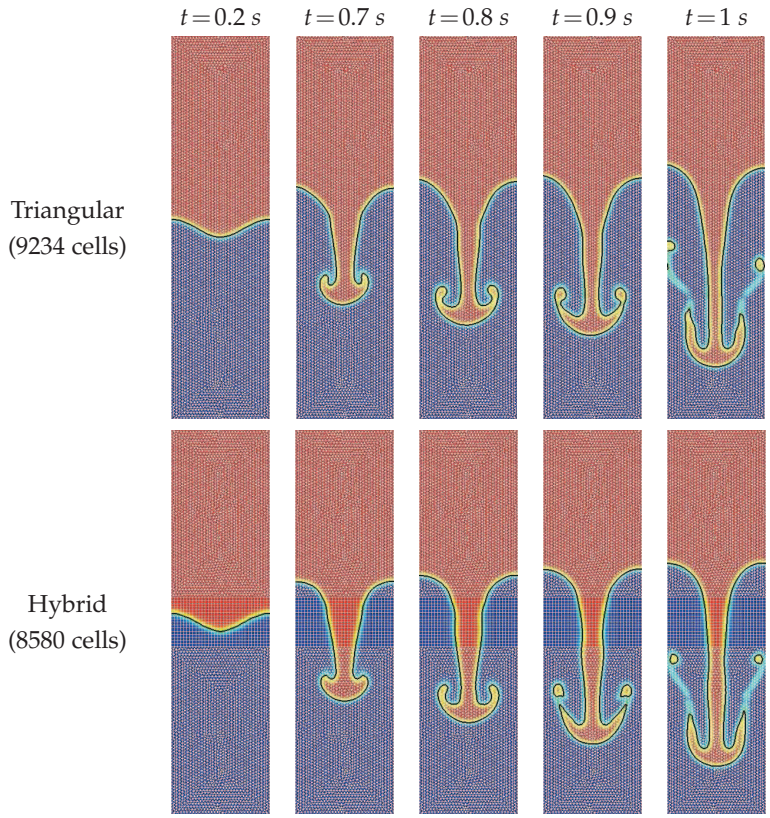

Figure 4: Volume fractions and interface (in black) predicted by *RCLSFoam* for the Rayleigh-Taylor instability — Comparison hybrid vs. triangular mesh (meshes overlaying the contours in white).

is due to the initialisation of the volume fraction field: whereas the sine interface is set on a perfectly symmetrical Cartesian mesh for the hybrid grid, it is initialised on a non-symmetrical mesh for the triangular grid. As the initialisation of the interface is critical to the symmetry of the solution, the results obtained on the hybrid mesh are more symmetrical. It is also worth noting that the progression of the mushroom-shaped structure in the triangular part of the hybrid mesh does not affect its symmetry. This also illustrates how one can take advantage of the ability to run on hybrid meshes and further highlights the relevance of this capability.

3.2.2 Falling drop in a pool

The settings for the simulation of the falling drop in a pool are given in [54] ("Impact of drop on water surface I" with $U=4\ ms^{-1}$). For this test case, the transport of the volume fraction φ was performed with *RCLSFoam* using the WENO scheme and setting the interface thickness parameter to $\epsilon=0.5\overline{\Delta x}$. This computation is challenging as it involves a density ratio of 816.

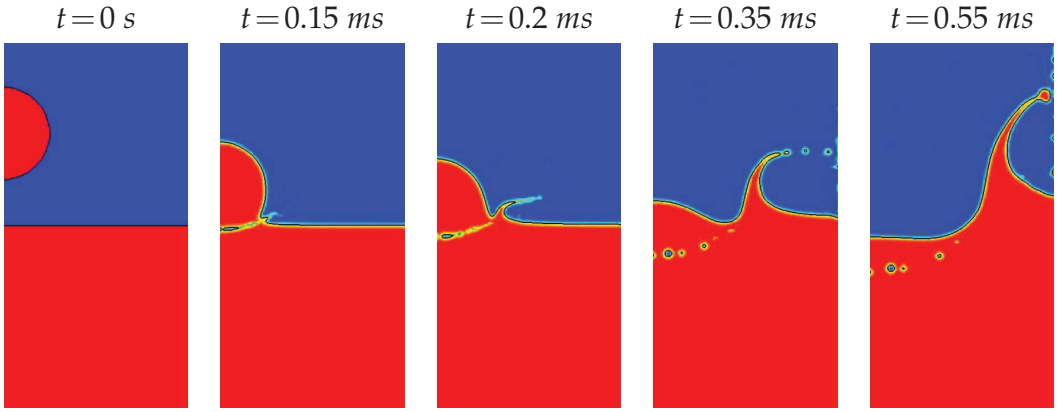

Figure 5: Volume fractions and interface (in black) predicted by *RCLSFoam* for the falling drop in a pool — Time $t=0\ s$,0.15 ms,0.2 ms,0.35 ms,0.55 ms.

For this computation, the solution of the pressure-velocity coupling is performed using a Crank-Nicholson (CN) temporal discretisation and the resulting systems of algebraic equations are solved with the generalised geometric-algebraic multi-grid solver (GAMG). Although this choice of numerics generally improves the accuracy (CN) and the speed (GAMG) of the computation, it significantly reduces the stability margin of the numerical method. Indeed, no stable computation was obtained for this test case with *interFoam* using either of these numerical methods. This further highlights the superior robustness of our modelling capability.

Fig. 5 presents the volume fractions and the interface predicted by *RCLSFoam* on a 128×256 Cartesian mesh for five different times in $[0;0.55]$ millisecond. It can be seen in the Fig. 5, that the *RCLSFoam* copes remarkably well with the very large density ratio and that the results match closely previous solutions (see [54]).

To conclude, in this section we have demonstrated that our modelling capability captures the physics well on various unstructured grids. We also showed that *RCLSFoam* conserves mass to machine accuracy. In addition, we have established that this multiphase modelling tool is very robust. Finally, it follows from these numerical tests that *RCLSFoam* outperforms *interFoam* in terms of accuracy and robustness.

4 Large eddy simulation of primary liquid-sheet breakup

4.1 The Quasi-DNS/LES approach

This numerical approach involves applying a single-phase LES formulation in both phases and extending it to the region of the interface. Due to the lack of established models, this approach neglects the sub-grid scale effects associated with the presence of the interface.

4.1.1 Filtered Navier-Stokes equations

The convolution of (2.32) and (2.33) with an homogeneous kernel filter G_Δ provides the following filtered incompressible Navier-Stokes equations:

$$\nabla\cdot\overline{\mathbf{u}}=0, \tag{4.1}$$

$$\frac{\partial(\rho\overline{\mathbf{u}})}{\partial t}+\nabla\cdot(\rho\overline{\mathbf{u}}\otimes\overline{\mathbf{u}})=-\nabla\overline{p}+\rho\mathbf{g}+\sigma\kappa\nabla\varphi+\nabla\cdot\left(2\mu\overline{\mathcal{D}}-\rho\mathcal{T}\right), \tag{4.2}$$

where:

- The filtered rate-of-strain tensor $\overline{\mathcal{D}}$ reads:

$$\overline{\mathcal{D}}=\frac{1}{2}\left(\nabla\overline{\mathbf{u}}+(\nabla\overline{\mathbf{u}})^T\right). \tag{4.3}$$

- The residual-stress tensor $\mathcal{T}$ is:

$$\mathcal{T}=\overline{\mathbf{u}\otimes\mathbf{u}}-\overline{\mathbf{u}}\otimes\overline{\mathbf{u}}. \tag{4.4}$$

- Following the principle of the quasi-DNS/LES approach, the sub-grid scale contributions of the capillary forces $\left(\mathbf{f_{cap}}\right)_{SGS}$ have been neglected:

$$\left(\mathbf{f_{cap}}\right)_{SGS}=\mathbf{0}=\sigma\kappa\nabla\varphi-\sigma\overline{\kappa\nabla\varphi}, \tag{4.5}$$

$$\sigma\overline{\kappa\nabla\varphi}=\sigma\kappa\nabla\varphi. \tag{4.6}$$

4.1.2 Residual kinetic energy

Filtering the kinetic energy field $E=\frac{1}{2}\mathbf{u}\cdot\mathbf{u}$ produces $\overline{E}$:

$$\overline{E}=\frac{1}{2}\overline{\mathbf{u}\cdot\mathbf{u}}. \tag{4.7}$$

Decomposing $\overline{E}$ into the kinetic energy of the filtered velocity field E_f and the residual kinetic energy k_r leads to [42]:

$$\overline{E}=E_f+k_r, \tag{4.8}$$

where k_r is expressed as:

$$k_r=\frac{1}{2}\overline{\mathbf{u}\cdot\mathbf{u}}-\frac{1}{2}\overline{\mathbf{u}}\cdot\overline{\mathbf{u}}. \tag{4.9}$$

Noting that $k_r=\frac{1}{2}\mathrm{tr}(\mathcal{T})$, the decomposition of the residual-stress tensor into an isotropic part and a deviatoric part $\mathcal{T}_D$ can be expressed as follows:

$$\mathcal{T}=\frac{2}{3}k_r\mathcal{I}+\mathcal{T}_D, \tag{4.10}$$

where $\mathcal{I}$ is the unit tensor.

4.1.3 Sub-grid scale modelling

For this computation, we have chosen to model the sub-grid scale stress tensor $\mathcal{T}$ with the constant coefficient one-equation eddy-viscosity model (OEEVM) proposed by Yoshizawa [67]. The OEEVM is based on Boussinesq's eddy-viscosity concept which postulates that the mechanism governing the transfer of energy from the resolved scales to the residual scales is analogous to the mechanism driving the molecular diffusion.

As the balance between the rate of production of the residual kinetic energy and the rate of dissipation of kinetic energy breaks down near walls and in jets and wakes, Yoshizawa proposed a model equation for the residual kinetic energy k_r. Yoshizawa derives a modelled form of this equation by using the statistical results from the direct-interaction approximation [29–31]. This statistical approach assumes the distinct separation of the grid-scales mean motions and the sub-grid scale fluctuating motions [66, 68]. Introducing the eddy-viscosity of the residual motions ν_r and noting ε_{k_r} the dissipation term, the model transport equation for the residual kinetic energy reads:

$$\frac{\partial k_r}{\partial t}+\nabla\cdot(\overline{\mathbf{u}}k_r)=\nabla\cdot((\nu_r+\nu)\nabla k_r)-\varepsilon_{k_r}-\overline{\mathcal{D}}:\mathcal{T}, \tag{4.11}$$

where ε_{k_r} is modelled as:

$$\varepsilon_{k_r}=\frac{C_\epsilon k_r^{\frac{3}{2}}}{\Delta}. \tag{4.12}$$

Yoshizawa's model performs relatively well on the types of flow encountered in atomisation problems while remaining significantly cheaper than more advanced SGS models [18].

4.2 Computation results

As the emphasis of this numerical study is placed on the mechanisms driving the primary breakup, the computational domain is limited to the close vicinity of the injection plane.

4.2.1 Settings of the computation

Domain and material properties In order to demonstrate the modelling capability on a test case reproducing the breakup mechanisms observed at aero-engine conditions, we have chosen to compute flat sheet breakup at $We=9300$.

Computational domain The computational domain is a cuboid of $3\times1\times1$ mm^3, meshed with 2.36×10^6 cells. In order to demonstrate the capability on general polyhedral meshes, the grid is made of 8.07×10^5 hexahedra, 1.5×10^6 tetrahedra and 5.4×10^4 pyramids (see bottom picture in Fig. 6).

The gas and fuel injection channels are modelled and the thickness of the plates separating the injection channels is resolved (see top picture in Fig. 6). Both of these features have proven to be of significant importance in the numerical simulation of primary

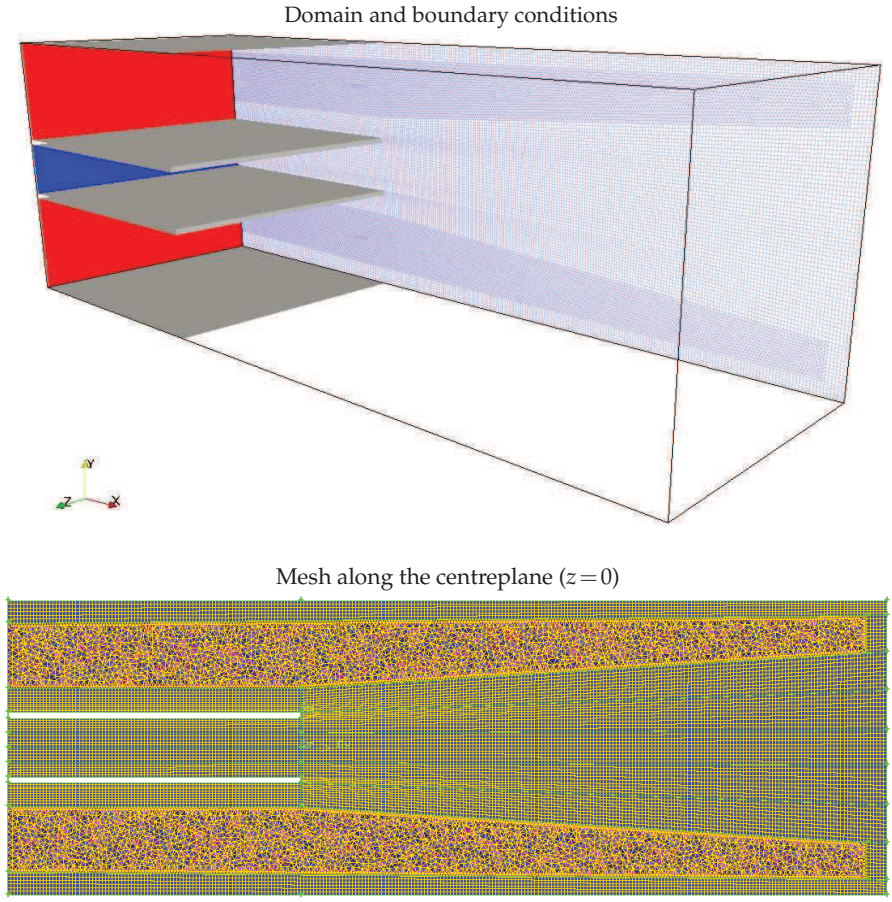

Figure 6: Computational domain for the simulation of atomisation — In the top half: the mesh of the back plane (edges in blue) and the boundaries (walls in grey, fuel inlet in blue and gas inlets in red) are pictured.

breakup [19]. The geometrical details of the injection configuration can be found in Table 2.

The front and back planes — respectively defined by $z=0.5\ mm$ and $z=-0.5\ mm$ (see top picture in Fig. 6) — are set as symmetric boundary conditions. The plane at $x=0$ is the inlet of the computational domain. In the central part of this plane — between the two plates — the fuel ($\varphi=1$) is injected at a speed of 2 ms^{-1}. Above and below the fuel injection channel, the gas ($\varphi=0$) enters the domain at a speed of 40 ms^{-1}. The rest of the boundaries are defined as inlet/outlet boundary conditions.

In order to take advantage of the ability to run on hybrid meshes, structured hexahedral grids have been fitted around walls. Similarly, to improve the accuracy of the atomisation modelling, the regions where the breakup is expected to occur have been meshed with hexahedral cells. Due to issues experienced with the inlet/outlet boundary conditions in OpenFOAM, these boundaries have also been meshed with hexahedra.

Table 2: Geometrical parameters for the spray calculation.

	Flat sheet
Configuration	prismatic
Nozzle outlet shape	rectangle (h)
Nozzle outlet dimension	$2\times10^{-4}\ m$
Separating plates thickness	$2\times10^{-5}\ m$
Domain tangential extent	width $W=5h$
Domain radial extent	height $H=5h$
Channel length	$5h$
Domain length	$15h$

The rest of the domain is composed of tetrahedra and pyramids. The pyramidal mesh consists of a single layer of cells performing the transition between the hexahedral and the tetrahedral meshes. In the resulting mesh, the smallest edge length is $\Delta x_{min}=5\ \mu m$ and the average characteristic length scale of the grid is $\overline{\Delta x}=8.4\ \mu m$.

Material properties Although the material properties chosen for this study (see Table 3) differ slightly from those of an aero-engine, the physical quantities remain similar. The non-dimensional numbers related to this computation are given in Table 4 and the smallest length scales associated with the flow field are reported in Table 5.

Considering that a given length scale η is resolved if $\eta\geq2\Delta x$, it can be seen in Table 5 that only the Kolmogorov length scale in the liquid phase η_{liq} is properly resolved by the mesh. This justifies the use of a sub-grid scale model for the turbulence in the gas phase. Table 5 also suggests that the mesh is far from resolving the smallest liquid structures produced. This further highlights the need to develop sub-grid scale models for multiphase flows.

Table 3: Physical properties for the spray calculation.

		Fuel	Gas	Ratio fuel/gas
Density, ρ	(kgm^{-3})	840	20	42
Viscosity, μ	$(kgm^{-1}s^{-1})$	5×10^{-3}	1.7×10^{-5}	294
Surface tension, σ	(Nm^{-1})	2.61×10^{-2}		

Table 4: Non-dimensional numbers associated to the flow simulated.

Re_{liq}	67
Re_{gas}	18800
We	9300
Oh	7.55×10^{-2}

Table 5: Smallest length scale of the flow field — assuming a turbulence intensity of 5% in the liquid and 10% in the gas.

Liquid phase Kolmogorov scale, η_{liq}	81 μm
Gas phase Kolmogorov scale, η_{gas}	1.4 μm
Droplet diameter at $We=10$, $d_{We=10}$	0.22 μm
Minimum mesh size, Δx_{min}	5 μm
Average mesh size, $\overline{\Delta x}$	8.4 μm

RCLS settings In the interest of robustness and because atomisation problems involve large density ratios, we choose to use the WENO scheme for this calculation. Although our numerical scheme [46] can formally reach arbitrarily high order in space, in this demonstration of the modelling capability we limit ourselves to a third-order polynomial reconstruction: $r=3$, leading to a fourth-order accurate WENO scheme.

To ensure the stability of the computation with an optimum resolution of thin ligaments, this computation features $\epsilon=0.5\overline{\Delta x}$ on the whole computational domain and the periodicity of the re-initialisation is set to $N_s=5$. The chosen set of RCLS parameters is summarised in Table 6.

Table 6: RCLS parameters for the simulation of atomisation.

Order of the polynomial reconstruction:	$r=3$
Numerical scheme:	WENO
CLS coefficient:	$\epsilon=0.5\overline{\Delta x}$
Periodicity of the re-initialisation:	$N_s=5$

4.2.2 Torn sheet breakup

Sheet breakup regimes Fernandez et al. studied the breakup of a flat sheet of water (300 μm thick, $U_{liq}\in[1;2]\ ms^{-1}$) sheared on either side by a stream of gas ($U_{gas}\in[20;70]\ ms^{-1}$, $p_{gas}\in[1;6]\ bar$) [17]. In their experimental analysis, the authors classify the regime of the primary breakup according to the momentum flux ratio M. Using the subscripts gas and liq to refer to the gas and liquid phases respectively, the momentum flux ratio M reads:

$$M=\frac{\rho_{gas}U_{gas}^2}{\rho_{liq}U_{liq}^2}. \tag{4.13}$$

In particular, Fernandez et al. identified three regimes of liquid sheet breakup:

Up to $M=0.5$: Cellular breakup. This regime is characterised by the formation of cell-like structures in the liquid sheet through the build-up of longitudinal and transverse undulations of similar wavelength. Such a combination of undulations leads to the

bursting of the membranes associated with the cell-like structures and to the creation of spanwise ligaments.

From $M=0.5$ **to** $M=5$ Stretch streamwise ligament breakup. Similarly to the cellular breakup, this regime involves the build-up of both longitudinal and transverse undulations. However, for this regime the fragmentation of the sheet occurs along the longitudinal direction such that the bursting of the membranes is accompanied with the creation of streamwise ligaments.

Above $M=5$**:** Torn sheet breakup. As for the previous breakup regime, the torn sheet breakup produces droplets through the disintegration of membranes and via the fragmentation of streamwise ligaments. However, the streamwise ligaments formed have highly irregular shapes and disintegrate through aerodynamic tearing rather than Plateau-Rayleigh instability. This regime also involve the tearing of the continuous region of the liquid sheet into large liquid structures further fragmented by the aerodynamic forces.

In our simulation of the primary breakup, the momentum flux ratio is: $M=9.5$. According to the above classification, this value of M puts the calculation in the regime of torn sheet breakup. The flow features predicted by our simulation for this breakup regime are reported in Figs. 7 to 11.

Interaction with vortices The figures of this sub-section present the liquid phase together with an ad hoc iso-surface of the Q-criterion [25] to illustrate the interaction of the turbulence with the liquid sheet. The Q-criterion — defined as the second invariant of the velocity gradient tensor — is widely used to visualise the coherent vortical structures in the flow field [12, 14]. The scalar field Q is given by:

$$Q=\frac{1}{2}\Big((\mathrm{tr}(\nabla\mathbf{u}))^2-\mathrm{tr}(\nabla\mathbf{u}\cdot\nabla\mathbf{u})\Big). \tag{4.14}$$

Due to the difference in velocity between the two phases, a shear layer appears on the interface. As a result, a Kelvin-Helmoltz (KH) instability builds up and — as can be seen in Figs. 7 to 11 — KH rollers form on either side of the liquid sheet, following initially the shape of the phase interface. As these vortices progress through the computational domain, they break up, thus increasing the level of turbulence downstream of the bulk liquid.

The Kelvin-Helmholtz vortices evolve in shape as the interface deforms. Initially, the sheet undulates in the longitudinal direction such that these spanwise turbulent structures remain more or less cylindrical (see Fig. 8 at $t=1.09$ *ms*). As the instabilities develop in the transverse direction the KH vortices present more corrugated and bended shapes (see Fig. 8 at $t=1.145$ *ms*).

At $t=1.25$ *ms*, the transverse deformation of the liquid sheet appears closer to the injection point, resulting in the formation of a hump right at the outlet of the top gas

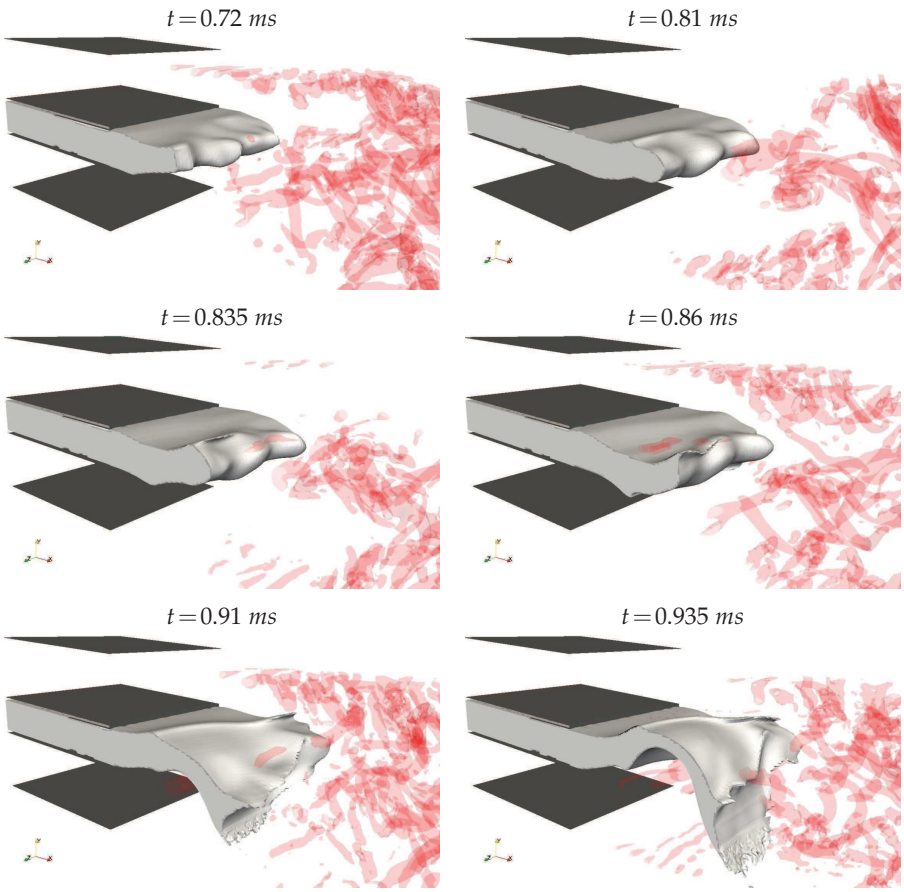

Figure 7: Simulation of flat sheet breakup with *lesRCLSFoam* — Liquid phase (in grey) and an ad hoc iso-surface of Q-criterion (in transparent red) for the build-up of instabilities.

injection channel (see Fig. 10). As a result, worm-like structures form behind and around the hump. These structures are principally aligned with the spanwise direction.

Later on, at t=1.29 ms, flat turbulent structures form on top of the protruding interface (see Fig. 10). Similar eddies were observed by Desjardins in his numerical simulation of a planar liquid jet in quiescent air [12]. Desjardins related the formation of these flat eddies to re-circulation regions above the corrugations of the interface. In line with the phenomenological analysis of Wu and Faeth [65], this process generates a lift that further increases the deformation of the interface [12].

Evolution of the liquid sheet The simulation of sheet breakup involves three main phases:

- The build-up of instabilities on the two interface surfaces ($t < 0.935\ ms$).

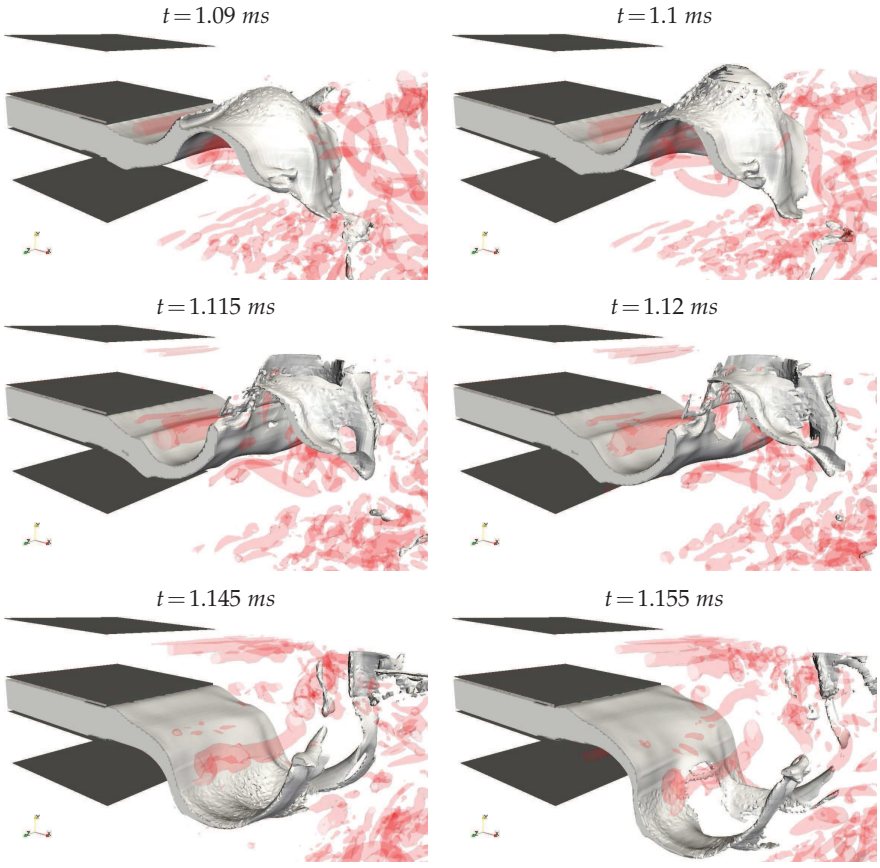

Figure 8: Simulation of flat sheet breakup with *lesRCLSFoam* — Liquid phase (in grey) and an ad hoc iso-surface of Q-criterion (in transparent red) for the flapping, the membrane puncturing and the ligament formation.

- The flapping of the sheet in the longitudinal and transverse directions ($t \in [0.935;1.25]\ ms$).
- The tearing of the liquid sheet ($t > 1.25\ ms$).

Build-up of instabilities This phase starts with the penetration of the liquid in the computational domain and finishes with the first occurrence of the breakup at $t = 0.935\ ms$. It involves the initial deformation of the interface in the injection channel and the development of sinuous and varicose modes of undulation of the liquid sheet (see Fig. 7). The growth of surface waves — in both the longitudinal and the transverse directions — leads to the thinning of the liquid sheet, thus facilitating the first pinch-off event by aerodynamic tearing.

Sheet flapping This phase involves the flapping of the sheet in both the longitudinal and the transverse directions, similarly to a flag. For this stage, the simulation predicts

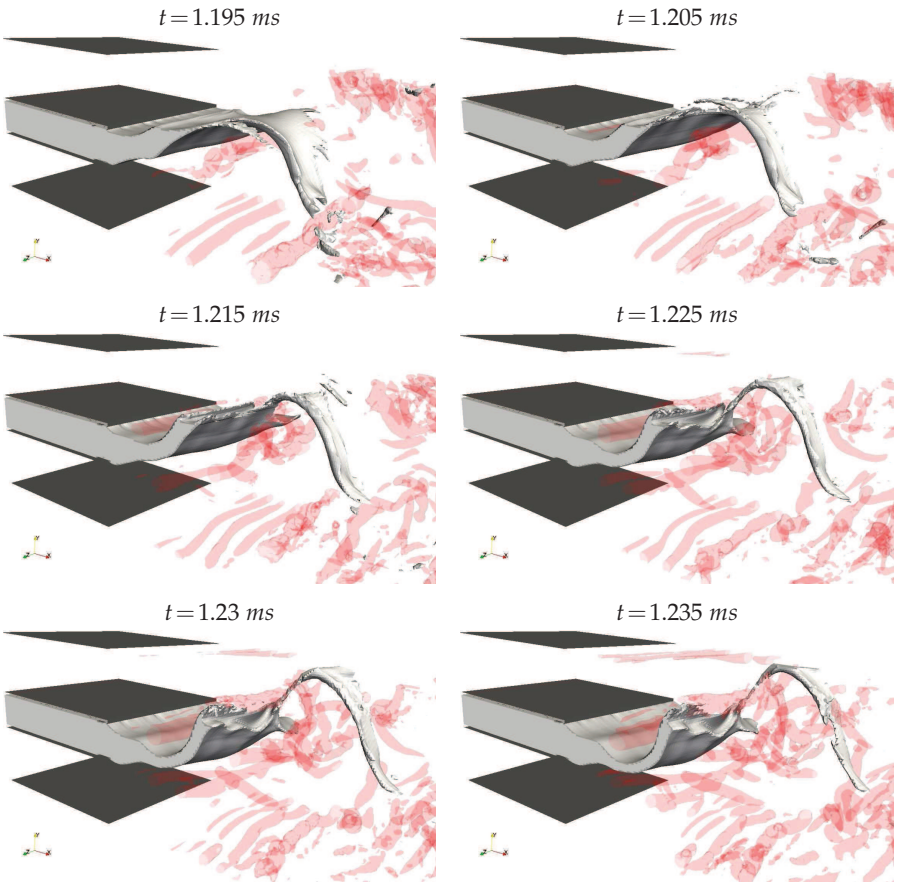

Figure 9: Simulation of flat sheet breakup with *lesRCLSFoam* — Liquid phase (in grey) and an ad hoc iso-surface of Q-criterion (in transparent red) for the pinch-off of a streamwise ligament.

the disintegration of the membranes formed at the peaks and the troughs of the undulations (see Fig. 8). The membrane puncturing is accompanied by the formation and the pinch-off of streamwise ligaments (see Fig. 9). These flow features suggest that the breakup regime is the stretch streamwise ligament breakup. It constitutes a transition before the establishment of torn sheet breakup.

Sheet tearing From $t = 1.25\ ms$, the computation predicts the tearing of the sheet in the transverse and then the longitudinal directions (see Fig. 10 and Fig. 11 respectively).

At $t = 1.25\ ms$, the liquid sheet presents a bag-like structure bent towards the top of the domain. As the sheet significantly obstructs the gas stream, it is subjected to relatively high aerodynamic forces and a tear is initiated. While the tear propagates in the transverse direction — following the path of minimum sheet thickness — the liquid structure being torn away undergoes a membrane-type breakup.

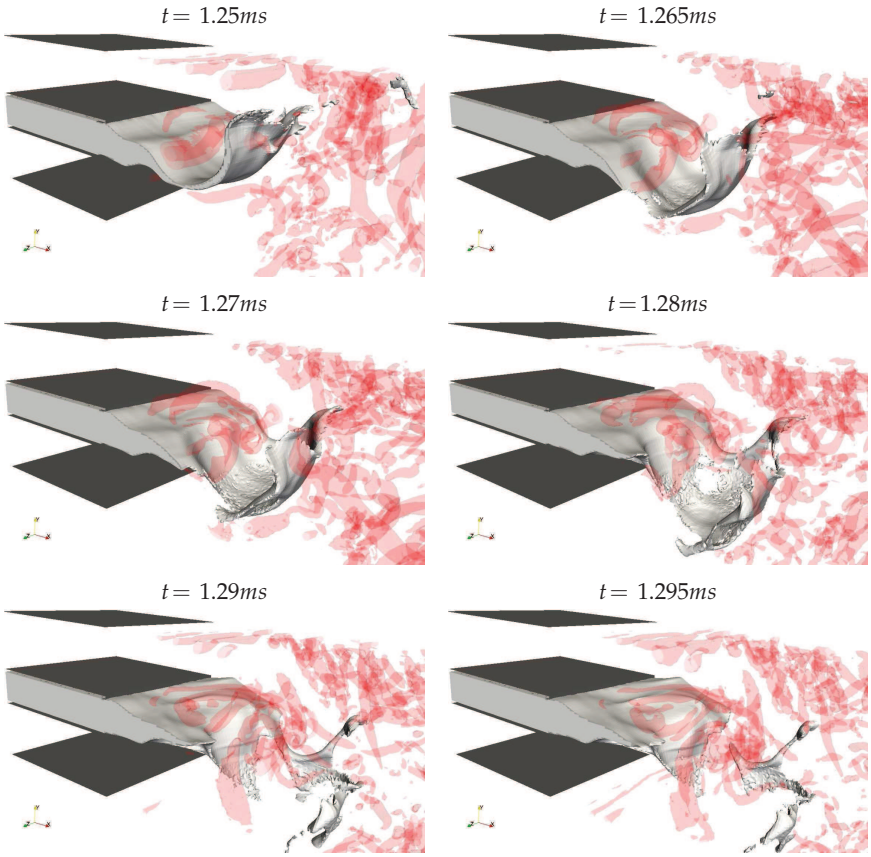

Figure 10: Simulation of flat sheet breakup with *lesRCLSFoam* — Liquid phase (in grey) and an ad hoc iso-surface of Q-criterion (in transparent red) for the tearing of the sheet in the transverse direction.

Then, at time $t = 1.3$ ms, a bag-like structure is formed in the centre of the sheet. This structure is punctured and the aerodynamic forces initiate a longitudinal tear in the hole produced. As the tear propagates upstream in the liquid phase, two streamwise ligaments are formed. These ligaments develop bag-like structures themselves and get subsequently torn away by the gas stream.

The flow field predicted by the numerical simulation in the "sheet tearing" phase matches closely the description of torn sheet breakup given in [17]. This validates qualitatively our simulation of the liquid sheet breakup. Our computation of the liquid sheet breakup highlights the potential of the numerical approach to study the mechanisms of the primary breakup.

4.2.3 Breakup length

As a first step towards a quantitative validation of this numerical simulation of sheet breakup, the average breakup length predicted by the computation is compared to the

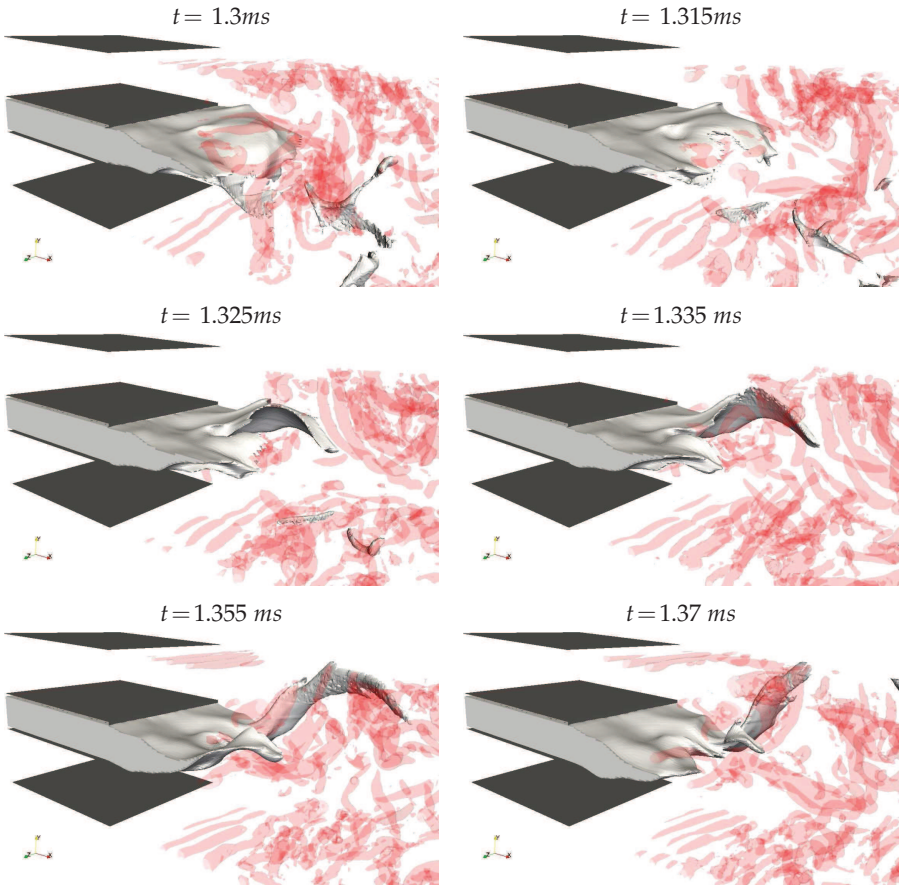

Figure 11: Simulation of flat sheet breakup with *lesRCLSFoam* — Liquid phase (in grey) and an ad hoc iso-surface of Q-criterion (in transparent red) for the tearing of the sheet in the longitudinal direction.

value given by the correlation provided in [17]. We performed the averaging over the entire span once the breakup regime was established.

In [17], the authors relate the breakup length L_b to a non-dimensional number. Recalling that h is the height of the fuel injection channel and noting We_h, the Weber number based on h, this relation reads:

$$\frac{L_b}{h} = f\left(\sqrt[3]{\frac{\frac{U_{liq}}{U_{gas}}}{MWe_h}}\right). \tag{4.15}$$

For the conditions of the calculation, the non-dimensional number is equal to 0.008, which leads to $\frac{L_b}{h} = 6 \pm 2$. In our numerical experiment, we observe an average breakup length of $\overline{\frac{L_b}{h}} = 5$ which is well within the range predicted by the correlation.

It is also worth noting that (4.15) is based on a restricted range of flow conditions (water liquid sheet; air pressure below 6 *bar*), and that it accounts for a limited range of parameters (ignores Re_{liq}). A correlation based on a more exhaustive experimental test campaign may further confirm the prediction of our simulation.

5 Conclusion

The Conservative Level Set (CLS) method of Olsson et al. [37, 38] was chosen as starting point for our novel interface description technique because this technique conserves mass well at a lower cost than hybrid methods [21], resolves the interface accurately as it is based on a level set formulation and has been demonstrated on the atomisation of Diesel jet (simple configuration) by Desjardins [13]. However, the conservative level set method needed to be improved in terms of stability and accuracy. It was also necessary to extend it to unstructured grids.

The extension to general polyhedral meshes and the improvement in terms of stability were obtained by solving the advection equation and the re-initialisation equation of the CLS method with the WENO scheme presented in [45, 46]. In particular, this numerical scheme significantly improved the stability of the method in the presence of very large density ratios as demonstrated by the simulation of the falling droplet (see Section 3.2.2). For this calculation, our modelling capability remained stable regardless of the numerics employed to solve the pressure-velocity coupling.

The improvement of the accuracy of the CLS method originated from two sources: the high-order accurate numerical scheme and the addition of a flux-limiter algorithm to the transport of the level set scalar. This additional step insures that the solution remains bounded.

Whereas the conservative level set methods of Olsson et al. and Desjardins et al. treat the scalar field as a level set, we choose to consider it as a smeared out liquid volume fraction. The addition of the flux limiter, specific to VOF methods, extends the CLS further towards a volume of fluid method and guarantees that the liquid volume fraction remains physical everywhere in the computational domain ($0 \leq \varphi \leq 1$). The resulting method named Robust Conservative Level Set conserves mass to machine accuracy (see Section 3.2.1) and captures the physics accurately (see Section 3.2).

Our new modelling capability has also been demonstrated on the simulation of the primary breakup of a liquid sheet in a co-flowing stream of gas. The calculation was performed using a quasi-DNS/LES methodology [21] (see Section 4.1) and the problem was formulated with material properties and boundary conditions relevant to the injection of fuel in an aero-engine combustor (see Section 4.2.1). The computation has demonstrated the ability of the modelling tool to capture the physics accurately (see Section 4.2) and further illustrates the potential of the numerical approach. The numerical results have been validated qualitatively against theoretical predictions (stability analysis) [1, 9] and experimental data [17].

Acknowledgments

This work has been funded by Rolls-Royce Group plc.

A Multidimensional universal limiter with explicit solution

A.1 Overview of the method

Multidimensional universal limiter with explicit solution (MULES) calculates a limited flux through the face F_l, $\widehat{F}_{L,l}$, for the liquid volume fraction φ such that for each cell E_i, the conservative level set at time t_{n+1}, $\varphi_i^{(n+1)}$, remains bounded by the minimal and maximal values of the solution in its neighbouring cells E_{j_l} at the previous time step t_n:

$$\min_{j_l}\left(\varphi_{j_l}^{(n)}\right)\leq\varphi_i^{(n+1)}\leq\max_{j_l}\left(\varphi_{j_l}^{(n)}\right),\qquad j_l=1,\cdots,L_i. \tag{A.1}$$

Let us note $\varphi_{i,min}^{(n+1)}$ and $\varphi_{i,max}^{(n+1)}$, respectively the minimum and the maximum admissible values for $\varphi_i^{(n+1)}$ in (A.1). To ensure that no non-physical values will be propagated, both $\varphi_{i,min}^{(n+1)}$ and $\varphi_{i,max}^{(n+1)}$ are then clipped between 0 and 1, using the following clipping operator:

$$\text{clip}(x)=\max(\min(x,1),0). \tag{A.2}$$

MULES follows the basic principles of the Flux-Corrected Transport (FCT) method of Boris and Book [3–5], in the format described by Zalesak [69]. In order to satisfy the boundedness criteria (A.1), MULES calculates the limited flux $\widehat{F}_{L,l}$ through F_l face by face by taking the weighted average of two fluxes for φ:

- The flux computed with a first-order upwind scheme for the advection equation only: $\widehat{F}_{U,l}$. This flux leads to a bounded solution but is diffusive.
- The sum of the fluxes computed with the high-order scheme, $\widehat{F}_{HO,l}$, for both the advection equation and the re-initialisation equation. This flux leads to a high-order accurate solution that is not systematically bounded.

As the weighting varies from face to face, the FCT computation of the limited flux is non linear. Introducing the limiter factor λ_l — calculated for each face F_l of the mesh — the expression for the limited flux then reads:

$$\widehat{F}_{L,l}=(1-\lambda_l)\widehat{F}_{U,l}+\lambda_l\widehat{F}_{HO,l}. \tag{A.3}$$

Introducing the correction flux $\widehat{F}_{C,l}$ defined as the difference between $\widehat{F}_{HO,l}$ and $\widehat{F}_{U,l}$, the expression for the limited flux (A.3) can then be re-written as:

$$\widehat{F}_{L,l}=\widehat{F}_{U,l}+\lambda_l\widehat{F}_{C,l}. \tag{A.4}$$

Once the limiter factor computed and the limited flux calculated according to (A.4), the scalar field φ is updated using an Euler time integration, such that:

$$\varphi_i^{(n+1)} = \varphi_i^{(n)} - \frac{\Delta t}{|E_i|}\sum_{l=1}^{L_i}\widehat{F}_{L,l}. \tag{A.5}$$

A.2 Determination of the limiter factor

The limiter factor λ_l is calculated iteratively such that the boundedness condition (A.1) is satisfied. λ_l directly derives from the re-formulation of the condition (A.1) in terms of fluxes. The bounds for the liquid volume fraction in E_i at time t_{n+1} correspond, in terms of fluxes, to the maximum temporal variation of liquid volume in E_i, $\left(\frac{\Delta V_{liq}}{\Delta t}\right)_i$. Introducing $\varphi_{i,min}^{(n+1)}$ and $\varphi_{i,max}^{(n+1)}$, respectively the maximum decrease and increase of liquid volume in E_i, these temporal variations — homogeneous to a flux — read respectively:

$$\begin{cases} \left(\dfrac{\Delta V_{liq}}{\Delta t}\right)_i^{out_{max}} = \dfrac{\varphi_i^{(n)} - \varphi_{i,min}^{(n+1)}}{\Delta t}\cdot|E_i|, \\ \left(\dfrac{\Delta V_{liq}}{\Delta t}\right)_i^{in_{max}} = \dfrac{\varphi_{i,max}^{(n+1)} - \varphi_i^{(n)}}{\Delta t}\cdot|E_i|, \end{cases} \tag{A.6}$$

so that fluxes limited by the temporal variations in (A.6), will lead to a bounded solution for φ.

Weller's algorithm searches iteratively the maximum value of λ_l that satisfies the boundedness criterion. Starting from $\lambda_l^{(0)} = 1$ — i.e. $\widehat{F}_{L,l} = \widehat{F}_{HO,l}$ — which leads to a high-order accurate solution, the algorithm progressively increases the contribution of $\widehat{F}_{U,l}$ to the flux by reducing λ_l.

To achieve that, the fundamental principal of MULES is to split the sum of correction fluxes for a given cell E_i into the sum of outflow and the sum of inflow correction fluxes. Then, in each cell, and at a given iteration k of the algorithm, an average limiter factor $\left(\lambda_i^{out}\right)^{(k)}$ is defined for all the faces that support an outflow correction flux and another one $\left(\lambda_i^{in}\right)^{(k)}$ is defined for all the faces that support an inflow correction flux.

These average limiter factors are introduced in the boundedness conditions expressed in terms of fluxes. These conditions then read:

$$\left(\frac{\Delta V_{liq}}{\Delta t}\right)_i^{out_{max}} = \left(\lambda_i^{out}\right)^{(k)}\sum_{l,out}\widehat{F}_{C,l} - \sum_{l,in}\lambda_l^{(k-1)}\widehat{F}_{C,l} + \sum_{l=1}^{L_i}\widehat{F}_{U,l}, \tag{A.7}$$

$$\left(\frac{\Delta V_{liq}}{\Delta t}\right)_i^{in_{max}} = \left(\lambda_i^{in}\right)^{(k)}\sum_{l,in}\widehat{F}_{C,l} - \sum_{l,out}\lambda_l^{(k-1)}\widehat{F}_{C,l} - \sum_{l=1}^{L_i}\widehat{F}_{U,l}, \tag{A.8}$$

where the sums of outflow and inflow fluxes in E_i are calculated the following way for a given flux $\widehat{F}_l$:

$$\begin{cases} \displaystyle\sum_{l,out} \widehat{F}_l = \sum_{l=1}^{L_i} \max\left(\widehat{F}_l, 0\right), \\ \displaystyle\sum_{l,in} \widehat{F}_l = \sum_{l=1}^{L_i} \min\left(\widehat{F}_l, 0\right). \end{cases} \tag{A.9}$$

As a flux exiting a cell is positive, the sum of upwind fluxes $\widehat{F}_{U,l}$ on all the faces of E_i is then added on the r.h.s. of (A.7). Similarly, the sum of upwind fluxes is subtracted on the r.h.s. of (A.8).

The average limiter factors $\left(\lambda_i^{out}\right)^{(k)}$ and $\left(\lambda_i^{in}\right)^{(k)}$ are then calculated from (A.7) and (A.8) respectively.

Then, the algorithm takes as the limiter factor for the face F_l at the current iteration k, $\lambda_l^{(k)}$, the minimum of three values:

- The relevant average limiter factor in the one of the adjacent cells E_i: $\left(\lambda_i^{out}\right)^{(k)}$ if the correction flux through F_l is exiting E_i, $\left(\lambda_i^{in}\right)^{(k)}$ otherwise.
- The relevant average limiter factor in the other adjacent cell E_j: $\left(\lambda_j^{in}\right)^{(k)}$ if the correction flux through F_l is entering E_j, $\left(\lambda_j^{out}\right)^{(k)}$ otherwise.
- The limiter factor at the previous iteration: $\lambda_l^{(k-1)}$.

The algorithm iterates m times — with m specified by the user — to produce a final limiter factor $\lambda_l^{(m)}$ for each face F_l of the mesh.

References

[1] F. Barreras, Experimental study of the break-up and atomization of a planar liquid sheet, Ph.D. thesis, University of Zaragoza (1998).
[2] G. Bianchi, P. Pelloni, S. Toninel, R. Scardovelli, A. Leboissetier, S. Zaleski, Improving the knowledge of high-speed liquid jets atomization by using quasi-direct 3D simulation, Tech. Rep. 2005-24-089, Society of Automotive Engineers (2005).
[3] D. Book, J. Boris, K. Hain, Flux-Corrected Transport II: Generalization of the method, Journal of Computational Physics 18 (1975) 248–283.
[4] J. Boris, D. Book, Flux-Corrected Transport I: SHASTA, a fluid transport algorithm that works, Journal of Computational Physics 11 (1973) 38–69.
[5] J. Boris, D. Book, Flux-Corrected Transport III: Minimal-error FCT algorithms, Journal of Computational Physics 20 (1976) 397–431.
[6] A. Bourlioux, A coupled Level Set and Volume of Fluid algorithm for tracking material interfaces, Proceedings of the 6th International Symposium On Computationnal Fluid Dynamics 6 (1995) 15–22.

[7] J. Brackbill, D. Kothe, C. Zemach, A continuum method for modeling surface tension, Journal of Computational Physics 100 (1992) 335–354.
[8] Y. Chang, T. Hou, B. Merriman, S. Osher, A Level-Set formulation of Eulerian capturing methods for incompressible fluid flows, Journal of Computational Physics 124 (1996) 449–464.
[9] J. Cousin, C. Dumouchel, Effect of viscosity on linear instability of a flat liquid sheet, Atomization and Sprays 6 (1996) 563–576.
[10] E. de Villiers, A. Gosman, H. Weller, Large eddy simulation of primary Diesel spray atomization, Tech. Rep. 2004-01-0100, Society of Automotive Engineers (2004).
[11] R. DeBar, A method in 2D Eulerian hydrodynamics, Tech. Rep. UCID-19683, Lawrence Livermore National Laboratory (1974).
[12] O. Desjardins, Numerical methods for liquid atomization and application in detailed simulations of a diesel jet, Ph.D. thesis, Stanford University (2008).
[13] O. Desjardins, V. Moureau, E. Knudsen, M. Herrmann, H. Pitsch, Conservative Level Set/ghost fluid method for simulating primary atomization, Proceedings of the 20th Annual Conference of the Institute for Liquid Atomization and Spray Systems - Americas.
[14] Y. Dubief, F. Delcayre, On coherent-vortex identification in turbulence, Journal of Turbulence 1 (2000) 1–22.
[15] M. Dumbser, M. Käser, Arbitrary high order non-oscillatory finite volume schemes on unstructured meshes for linear hyperbolic systems, Journal of Computational Physics 221 (2007) 693–723.
[16] D. Enright, R. Fedkiw, J. Ferziger, I. Mitchell, A hybrid Particle Level Set method for improved interface capturing, Journal of Computational Physics 183 (2002) 83–116.
[17] V. Fernandez, P. Berthoumie, L. G., Liquid sheet disintegration at high pressure: An experimental approach, Comptes Rendus Mécanique 337 (2009) 481–491.
[18] C. Fureby, G. Tabor, H. Weller, A. Gosman, A comparative study of subgrid scale models in homogeneous isotropic turbulence, Physics of Fluids 9 (1997) 1416–1429.
[19] D. Fuster, A. Bague, T. Boeck, L. Le Moyne, A. Leboissetier, S. Popinet, P. Ray, R. Scardovelli, S. Zaleski, Simulation of primary atomization with an octree adaptive mesh refinement and VOF method, International Journal of Multiphase Flow 35 (2009) 550–565.
[20] J. Glimm, O. McBryan, R. Menikoff, D. Sharp, Front tracking applied to Rayleigh-Taylor instability, SIAM Journal on Scientific and Statistical Computing 7 (1987) 230–251.
[21] M. Gorokhovski, M. Herrmann, Modeling primary atomization, Annual Review of Fluid Mechanics 2008 40 (2008) 343–366.
[22] C. Hirt, A. Amsden, J. Cook, An arbitrary Lagrangian-Eulerian computing method for all speeds, Journal of Computational Physics 14 (1974) 227–253.
[23] C. Hirt, B. Nichols, Volume of Fluid method for the dynamics of free boundaries, Journal of Computational Physics 39 (1981) 323–345.
[24] C. Hu, C.-W. Shu, Weighted essentially non-oscillatory schemes on triangular meshes, Journal of Computational Physics 150 (1999) 97–127.
[25] J. Hunt, A. Wray, P. Moin, Eddies, streams and convergence zones in turbulent flows, Tech. Rep. CTR-S88, Center for Turbulence Research (1988).
[26] R. Issa, Solution of the implicitly discretised fluid flow equations by Operator-Splitting, Journal of Computational Physics 62 (1985) 40–65.
[27] D. Jacqmin, An energy approach to the continuum surface tension method, Tech. Rep. 96-0858, American Institute of Aeronautics and Astronautics (1996).
[28] D. Kim, O. Desjardins, M. Herrmann, P. Moin, The primary breakup of a round liquid jet by

a coaxial flow of gas, Proceedings of the 20th Annual Conference of the Institute for Liquid Atomization and Spray Systems - Americas.
[29] R. Kraichnan, The structure of isotropic turbulence at very high Reynolds numbers, Journal of Fluid Mechanics 5 (1959) 497–543.
[30] R. Kraichnan, Direct-interaction approximation for shear and thermally driven turbulence, Physics of Fluids 7 (1964) 1048–1062.
[31] R. Kraichnan, Eulerian and Lagrangian renormalization in turbulence theory, Journal of Fluid Mechanics 83 (1977) 349–374.
[32] P. Lax, B. Wendroff, Systems of conservation laws, Communications on Pure and Applied Mathematics 13 (1960) 217–237.
[33] J. Lopez, J. Hernandez, P. Gomez, F. Faura, An improved PLIC-VOF method for tracking thin fluid structures in incompressible two-phase flows, Journal of Computational Physics 208 (2005) 51–74.
[34] J. Magnaudet, M. Rivero, J. Fabre, Accelerated flows past a rigid sphere or a spherical bubble. part I Steady straining flow, Journal of Fluid Mechanics 284 (1995) 97–135.
[35] T. Menard, S. Tanguy, A. Berlemont, Coupling Level Set/VOF/ghost fluid methods: Validation and application to 3D simulation of the primary break-up of a liquid jet, International Journal of Multiphase Flow 33 (2007) 510–524.
[36] W. Noh, P. Woodward, SLIC (simple line interface calculation), Proceedings of the Fifth International Conference on Numerical Methods in Fluid Dynamics Springer-Verlag New York 59 (1976) 330–340.
[37] E. Olsson, G. Kreiss, A conservative level set method for two phase flow, Journal of Computational Physics 210 (2005) 225–246.
[38] E. Olsson, G. Kreiss, S. Zahedi, A conservative level set method for two phase flow II, Journal of Computational Physics 225 (2007) 785–807.
[39] OpenCFD Ltd, OpenFOAM, User Guide, version 1.5 (July 2008).
[40] S. Osher, R. Fedkiw, Level Set Methods and Dynamic Implicit Surfaces, Applied Mathematical Sciences, 153, New York: Springer, 2002.
[41] S. Osher, J. Sethian, Fronts propagating with curvature-dependent speed: Algorithms based on Hamilton-Jacobi formulations, Journal of Computational Physics 79 (1988) 12–49.
[42] S. Pope, Turbulent Flows, Cambridge University Press, 2000.
[43] S. Popinet, S. Zaleski, A front tracking algorithm for the accurate representation of surface tension, International Journal for Numerical Methods in Fluids 30 (1999) 775–779.
[44] T. Pringuey, Large eddy simulation of primary liquid-sheet breakup, Ph.D. thesis, University of Cambridge (2012).
[45] T. Pringuey, R. Cant, High order schemes on 3D mixed-element unstructured meshes, Tech. Rep. CUED/A-AERO/TR29, University of Cambridge, Department of Engineering (2010).
[46] T. Pringuey, R. Cant, High order schemes on three-dimensional general polyhedral meshes — Application to the level set method, Communications in Computational Physics 12 (2012) 1–41.
[47] E. Puckett, A. Almgren, J. Bell, D. Marcus, W. Rider, A high order projection method for tracking fluid interfaces in variable density incompressible flows, Journal of Computational Physics 130 (1997) 269–282.
[48] H. Rusche, Dispersed two-phase flows at high phase fractions, Ph.D. thesis, Imperial College of Science, Technology & Medicine (2002).
[49] G. Ryskin, L. Leal, Numerical solution of free boundary problems in fluid mechanics. part I The finite-difference technique, Journal of Fluid Mechanics 148 (1984) 1–17.

[50] R. Scardovelli, S. Zaleski, Direct numerical simulation of free-surface and interfacial flow, Annual Review of Fluid Mechanics 31 (1999) 567–603.
[51] J. Sethian, A fast marching Level Set method for monotonically advancing fronts, Proceedings of the National Academy of Science USA 93 (1996) 1591–1595.
[52] J. Sethian, Fast marching methods, SIAM Review 41 (1999) 199–235.
[53] C. Shu, S. Osher, Efficient implementation of essentially non-oscillatory shock-capturing schemes, Journal of Computational Physics 77 (1989) 439–471.
[54] M. Sussman, A. Almgren, J. Bell, P. Colella, L. Howell, M. Welcome, Adaptive Level Set approach for incompressible two-phase flows, Journal of Computational Physics 148 (1999) 81–124.
[55] M. Sussman, E. Fatemi, P. Smereka, S. Osher, An improved Level Set method for incompressible two phase flows, Computers and Fluids 27 (1998) 663–680.
[56] M. Sussman, E. Puckett, A coupled Level Set and Volume-of-Fluid method for computing 3D and axisymetric incompressible two-phase flows, Journal of Computational Physics 162 (2000) 301–337.
[57] M. Sussman, P. Smereka, S. Osher, A Level Set approach for computing solutions to incompressible two phase flow, Journal of Computational Physics 114 (1994) 146–159.
[58] V. Titarev, P. Tsoutsanis, D. Drikakis, WENO schemes for mixed-element unstructured meshes, Communications in Computational Physics 8 (2010) 585–609.
[59] G. Tryggvason, S. Unverdi, Computations of three-dimensional Rayleigh-Taylor instability, Physics of Fluids A 2 (1990) 656.
[60] P. Tsoutsanis, V. Titarev, D. Drikakis, WENO schemes on arbitrary mixed-element unstructured meshes in three space dimensions, Journal of Computational Physics 230 (2011) 1585–1601.
[61] S. Unverdi, G. Tryggvason, A front tracking method for viscous incompressible multi-fluid flows, Journal of Computational Physics 100 (1992) 25–37.
[62] S. Van der Pijl, A. Segal, A. Vuik, P. Wesseling, A mass-conserving Level Set method for modelling multi-phase flows, International Journal for Numerical Methods in Fluids 7 (2005) 339–361.
[63] R. Wang, R. Spiteri, Linear instability of the fifth-order WENO method, SIAM Journal on Numerical Analysis 45 (2007) 1871–1901.
[64] H. Weller, `http://www.opencfd.co.uk/openfoam/index.html#openfoam`.
[65] P. Wu, G. Faeth, Aerodynamic effects on primary breakup of turbulent liquids, Atomization and Sprays 3 (1993) 265–289.
[66] A. Yoshizawa, A statistically-derived subgrid model for the large-eddy simulation of turbulence, Physics of Fluids 25 (1982) 1532–1538.
[67] A. Yoshizawa, A statistically-derived subgrid-scale kinetic energy model for the large-eddy simulation of turbulent flows, Journal of the Physical Society of Japan 54 (1985) 2834–2839.
[68] A. Yoshizawa, Statistical theory for compressible turbulent shear flows, with the application to subgrid modeling, Physics of Fluids 29 (1986) 2152–2164.
[69] S. Zalesak, Fully multidimensional flux-corrected transport algorithms for fluids, Journal of Computational Physics 31 (1979) 335–362.
[70] Y.-T. Zhang, C.-W. Shu, Third order WENO scheme on three dimensional tetrahedral meshes, Communications in Computational Physics 5 (2009) 836–848.